NAVAL POSTGRADUATE SCHOOL
MONTEREY, CALIFORNIA

Original contains color plates: All DTIC reproductions will be in black and white

THESIS

AN INVESTIGATION OF THE TRANSONIC VISCOUS DRAG COEFFICIENT FOR AXI-SYMMETRIC BODIES

by

Yue Sang Fan

March, 1995

Thesis Advisor: Oscar Biblarz

Approved for public release; distribution is unlimited.

DISCLAIMER NOTICE

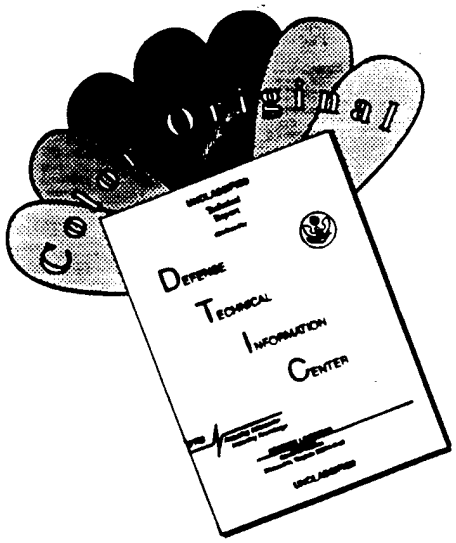

THIS DOCUMENT IS BEST QUALITY AVAILABLE. THE COPY FURNISHED TO DTIC CONTAINED A SIGNIFICANT NUMBER OF COLOR PAGES WHICH DO NOT REPRODUCE LEGIBLY ON BLACK AND WHITE MICROFICHE.

REPORT DOCUMENTATION PAGE

Form Approved OMB

1. AGENCY USE ONLY *(Leave blank)*	2. REPORT DATE March 1995.	3. REPORT TYPE AND DATES COVERED Master's Thesis

4. TITLE AND SUBTITLE AN INVESTIGATION OF THE TRANSONIC VISCOUS DRAG COEFFICIENT FOR AXI-SYMMETRIC BODIES

5. FUNDING NUMBERS

6. AUTHOR(S) Yue Sang Fan

7. PERFORMING ORGANIZATION NAME(S) AND ADDRESS(ES)
Naval Postgraduate School
Monterey CA 93943-5106

8. PERFORMING ORGANIZATION REPORT NUMBER

9. SPONSORING/MONITORING AGENCY NAME(S) AND ADDRESS(ES)

10. SPONSORING/MONITORING AGENCY REPORT NUMBER

11. SUPPLEMENTARY NOTES The views expressed in this thesis are those of the author and do not reflect the official policy or position of the Department of Defense or the U.S. Government.

12a. DISTRIBUTION/AVAILABILITY STATEMENT
Approved for public release; distribution is unlimited.

12b. DISTRIBUTION CODE

13. ABSTRACT *(maximum 200 words)*

Viscous drag in the transonic regime over an axi-symmetric body with a unique aft contour surface is investigated. The forebody is composed of an arbitrary ellipsoid. The unique aft contour surface has been obtained by an exact solution of the small perturbation transonic equation, using guidelines and tools developed at the Naval Postgraduate School. This unique contour allows the delay of shock formation in the aft portion, hence delaying the onset of wave drag which results in a reduction of the overall transonic pressure drag on the body. The drag coefficient thus computed is compared with another axi-symmetric body with the same ellipsoid forebody but a simple boat-tailed conical afterbody. Computational Fluid Dynamics (CFD) has been used to compute the viscous flow over the two bodies at zero incidence using a Navier-Stokes flow-solver. Results obtained confirm the advantage of the special shaped afterbody over the conical afterbody by showing the delayed formation of shock waves at the aft portion in transonic flow, consequently achieving a lower maximum drag coefficient of approximately 5.5%. These results can be used in the design low pressure-drag surfaces for shapes such as missiles, projectiles, aircraft external ferry tanks and aircraft engine nacelles for improved performance within the transonic flight regime.

14. SUBJECT TERMS Transonic viscous drag coefficient for axi-symmetric bodies

15. NUMBER OF PAGES 64

16. PRICE CODE

17. SECURITY CLASSIFICATION OF REPORT	18. SECURITY CLASSIFICATION OF THIS PAGE	19. SECURITY CLASSIFICATION OF ABSTRACT	20. LIMITATION OF ABSTRACT
Unclassified	Unclassified	Unclassified	UL

NSN 7540-01-280-5500

Standard Form 298 (Rev. 2-89)
Prescribed by ANSI Std. 239-18 298-102

Approved for public release; distribution is unlimited.

AN INVESTIGATION OF THE TRANSONIC VISCOUS DRAG COEFFICIENT FOR AXI-SYMMETRIC BODIES

Yue Sang Fan
Major, Republic of Singapore Air Force
B.S.(Hon), Manchester University, UK, 1988

Submitted in partial fulfillment
of the requirements for the degree of

MASTER OF SCIENCE IN AERONAUTICAL ENGINEERING

from the

NAVAL POSTGRADUATE SCHOOL
March 1995

Author: _____
Yue Sang Fan

Approved by: _____
Oscar Biblarz, Thesis Advisor

_____
Garth V. Hobson, Second Reader

_____
Daniel J. Collins, Chairman
Department of Aeronautics and Astronautics

ABSTRACT

Viscous drag in the transonic regime over an axi-symmetric body with a unique aft contour surface is investigated. The forebody is composed of an arbitrary ellipsoid. The unique aft contour surface has been obtained by an exact solution of the small perturbation transonic equation, using guidelines and tools developed at the Naval Postgraduate School. This unique contour allows the delay of shock formation in the aft portion, hence delaying the onset of wave drag which results in a reduction of the overall transonic pressure drag on the body. The drag coefficient thus computed is compared with another axi-symmetric body with the same ellipsoid forebody but a simple boat-tailed conical afterbody. Computational Fluid Dynamics (CFD) has been used to compute the viscous flow over the two bodies using a Navier-Stokes flow-solver. Results obtained confirm the advantage of the special shaped afterbody over the conical afterbody by showing the delayed formation of shock waves at the aft portion in transonic flow, consequently achieving a lower maximum drag coefficient of approximately 5.5%. These results can be used in the design of low pressure-drag surfaces for shapes such as missiles, projectiles, aircraft external ferry tanks and aircraft engine nacelles for improved performance within the transonic flight regime.

TABLE OF CONTENTS

ACKNOWLEDGEMENTS

I wish to thank my thesis advisor, Prof. O. Biblarz, for his patience, encouragement, support and guidance throughout the development of this thesis. I would also like to acknowledge the comments and suggestions made by Prof. G. Hobson on the CFD aspects of this thesis.

A special word of appreciation to my commanders in the Republic of Singapore Airforce and the Chief Defence Scientist for giving me this invaluable opportunity to enrich myself in the graduate program at the Naval Postgraduate School.

Finally, I would like to thank my wife, Swee Lian, and my daughter, Cuiwen, for their support, love and understanding which enabled me to focus my efforts into completing this thesis.

I. INTRODUCTION

The study of the aerodynamic characteristics of a missile-like object from launch to nominal flight speed will typically range from low subsonic to supersonic speeds. Entrenched within this range is a flight regime known as the transonic flight regime.

The study of transonic aerodynamics deserves individual treatment within the framework of gasdynamics. A typical transonic flow with a subsonic free-stream Mach number contains a supersonic zone, bounded by the sonic line and a shock wave, through which the flow decelerates back to subsonic flow. Transonic flows occurs typically within the free-stream Mach number range of $0.8 < M_\infty < 1.2$, depending on the shape of the object [Ref. 1].

Transonic aerodynamics is difficult to analyze or predict because it must be described by nonlinear equations. The transonic flow regime is also complicated by the formation of shock waves, the location of which depend on the complex interaction of free-stream Mach number and geometry of the body. This is in contrast to the purely subsonic or supersonic flow regimes where an adequate prediction of aerodynamic characteristics can be obtained using linear theory. Consequently, transonic flows are very sensitive to small perturbations in the various flow parameters such as Mach number and this makes accurate experimentation difficult [Ref. 1].

One of the main aerodynamic forces of interest is drag. Objects that achieve flight are designed with aerodynamic shapes. The prime objective of such designs is to obtain high lift and low drag. A condition associated with transonic flow is the significant increase in drag [Ref. 2]. Efforts to reduce the drag coefficient in the transonic regime must concentrate on reducing the pressure drag (inclusive of wave

drag) contributions to total drag. During wing design, one method to achieve lower drag is to use supercritical airfoil sections which are designed to delay the formation of a shock wave on the upper surface of the airfoil, thereby enabling a higher region of lift generation and a weaker shock to occur further downstream of the airfoil upper surface [Ref. 2].

A traditional approach to the investigation of aerodynamic characteristics is based on wind tunnel test data and actual flight test results. Unfortunately, both wind tunnel and flight testing are considerably expensive and time consuming. Furthermore, wind tunnel testing in the transonic regime requires special wind tunnels with adaptive walls in order to nullify possible reflected shock-interaction between the tunnel walls and the test object within the test section [Ref. 1]. As mentioned in Reference 1, it is also difficult to obtain highly reliable data from wind tunnel experimentations in the transonic flow regime.

In contrast, there has been much progress recently in the field of Computational Fluid Dynamics (CFD). The judicious use of CFD, in combination with the appropriate modelling, has enabled aerodynamicists to predict aerodynamic characteristics within a faster time frame and at relatively lower costs. Numerous codes are now available that run as both the Euler and Navier-Stokes flow-solvers [Ref. 3]. Many institutions are now using CFD as a "first-cut" predictor for improvements in aerodynamic designs or as a tool to extrapolate aerodynamic characteristics from known design performances. With the increased experience in CFD, such as better turbulence modelling and more efficient and robust codes, and with modern developments in high speed computing, one can expect to see an even larger proportion of aerodynamic design being accomplished using CFD.

II. TRANSONIC FLOW

Transonic flows are characterized by the simultaneous presence within the flow field of both subsonic and supersonic regions. The properties of transonic flows can be described using the equations of gas dynamics, namely, the equations of state, continuity, momentum and energy. If the object of interest is a slender body, we can use small perturbation theory to simplify the flow over the body [Ref. 2]. In fact, small perturbation theory can be applied throughout the entire Mach number range from low subsonic to supersonic speeds. Typically, the derivation is based on assumptions that the flow is steady, irrotational and isentropic with no energy transfer, no body forces and no shear stresses (i.e., inviscid flow).

A. SMALL PERTURBATION THEORY

For steady, isentropic and inviscid flow, the governing equations are

i) Continuity Equation

$$\frac{\partial(\rho u)}{\partial x}+\frac{\partial(\rho v)}{\partial y}+\frac{\partial(\rho w)}{\partial z}=0 \qquad (1)$$

Expanding and re-arranging equation (1)

$$\rho\frac{\partial u}{\partial x}+\rho\frac{\partial v}{\partial y}+\rho\frac{\partial w}{\partial z}=-\left(u\frac{\partial \rho}{\partial x}+v\frac{\partial \rho}{\partial y}+w\frac{\partial \rho}{\partial z}\right) \qquad (2)$$

ii) The Euler momentum equations are given by

$$u\frac{\partial u}{\partial x}+v\frac{\partial u}{\partial y}+w\frac{\partial u}{\partial z}=-\frac{1}{\rho}\frac{\partial p}{\partial x} \tag{3}$$

$$u\frac{\partial v}{\partial x}+v\frac{\partial v}{\partial y}+w\frac{\partial v}{\partial z}=-\frac{1}{\rho}\frac{\partial p}{\partial y} \tag{4}$$

$$u\frac{\partial w}{\partial x}+v\frac{\partial w}{\partial y}+w\frac{\partial w}{\partial z}=-\frac{1}{\rho}\frac{\partial p}{\partial z} \tag{5}$$

Since the flow is isentropic, we can express the speed of sound as

$$a^2=\frac{\partial p}{\partial \rho} \tag{6}$$

Multiplying the x-momentum equation (Eqn 3) by u yields

$$u^2\frac{\partial u}{\partial x}+uv\frac{\partial u}{\partial y}+uw\frac{\partial u}{\partial z}=-\frac{u}{\rho}\frac{\partial p}{\partial x}\frac{\partial \rho}{\partial \rho} \tag{7}$$

Substituting Eqn (6) into Eqn (7) yields

$$u^2\frac{\partial u}{\partial x}+uv\frac{\partial u}{\partial y}+uw\frac{\partial u}{\partial z}=-\frac{u}{\rho}\frac{\partial \rho}{\partial x}a^2 \tag{8}$$

Similarly, by multiplying the y-momentum and z-momentum equations by v and w respectively yields

$$uv\frac{\partial v}{\partial x}+v^2\frac{\partial v}{\partial y}+vw\frac{\partial v}{\partial z}=-\frac{v}{\rho}\frac{\partial \rho}{\partial y}a^2 \tag{9}$$

$$uw\frac{\partial w}{\partial x}+vw\frac{\partial w}{\partial y}+w^2\frac{\partial w}{\partial z}=-\frac{w}{\rho}\frac{\partial \rho}{\partial z}a^2 \tag{10}$$

Summing up Eqns (8), (9) and (10) gives

$$u^2\frac{\partial u}{\partial x}+uv\frac{\partial u}{\partial y}+uw\frac{\partial u}{\partial z}+uv\frac{\partial v}{\partial x}+v^2\frac{\partial v}{\partial y}+vw\frac{\partial v}{\partial z}+uw\frac{\partial w}{\partial x}+vw\frac{\partial w}{\partial y}+w^2\frac{\partial w}{\partial z}=$$

$$-\frac{a^2}{\rho}\left(u\frac{\partial \rho}{\partial x}+v\frac{\partial \rho}{\partial y}+w\frac{\partial \rho}{\partial z}\right) \qquad (11)$$

Substituting Eqn (2) into Eqn (11) yields

$$u^2\frac{\partial u}{\partial x}+uv\frac{\partial u}{\partial y}+uw\frac{\partial u}{\partial z}+uv\frac{\partial v}{\partial x}+v^2\frac{\partial v}{\partial y}+vw\frac{\partial v}{\partial z}+uw\frac{\partial w}{\partial x}+vw\frac{\partial w}{\partial y}+w^2\frac{\partial w}{\partial z}=$$

$$a^2\left(\frac{\partial u}{\partial x}+\frac{\partial v}{\partial y}+\frac{\partial w}{\partial z}\right) \qquad (12)$$

By rearranging Eqn (12), we obtain

$$\left(\frac{\partial u}{\partial x}-\frac{u^2}{a^2}\frac{\partial u}{\partial x}\right)+\left(\frac{\partial v}{\partial y}-\frac{v^2}{a^2}\frac{\partial v}{\partial y}\right)+\left(\frac{\partial w}{\partial z}-\frac{w^2}{a^2}\frac{\partial w}{\partial z}\right)$$

$$-\left(\frac{uv}{a^2}\frac{\partial u}{\partial y}+\frac{uv}{a^2}\frac{\partial v}{\partial x}\right)-\left(\frac{uw}{a^2}\frac{\partial u}{\partial z}+\frac{uw}{a^2}\frac{\partial w}{\partial x}\right)$$

$$-\left(\frac{vw}{a^2}\frac{\partial v}{\partial z}+\frac{vw}{a^2}\frac{\partial w}{\partial y}\right)=0 \qquad (13)$$

Since the flow is irrotational, we have

$$\frac{\partial u}{\partial y}=\frac{\partial v}{\partial x} \qquad (14)$$

$$\frac{\partial u}{\partial z}=\frac{\partial w}{\partial x} \qquad (15)$$

$$\frac{\partial w}{\partial y}=\frac{\partial v}{\partial z} \qquad (16)$$

Substituting Eqns (14), (15) and (16) into Eqn (13) and rearranging yields

$$\frac{\partial u}{\partial x}\left(1-\frac{u^2}{a^2}\right)+\frac{\partial v}{\partial y}\left(1-\frac{v^2}{a^2}\right)+\frac{\partial w}{\partial z}\left(1-\frac{w^2}{a^2}\right)$$

$$-2\frac{uv}{a^2}\frac{\partial u}{\partial y}-2\frac{uw}{a^2}\frac{\partial w}{\partial x}-2\frac{vw}{a^2}\frac{\partial v}{\partial z}=0 \qquad \textbf{(17)}$$

For a slender body moving in the x-direction, small perturbation theory gives the velocity field as

$$u=U_\infty+u' \; ; \; v=v' \; ; \; w=w' \qquad \textbf{(18)}$$

Since

$$u>u' \; ; \; u>v' \; ; \; u>w' \qquad \textbf{(19)}$$

We can simplify Eqn (17) to

$$\left(1-\frac{u^2}{a^2}\right)\frac{\partial u}{\partial x}+\frac{\partial v}{\partial y}+\frac{\partial w}{\partial z}=0 \qquad \textbf{(20)}$$

iii) The flow is isentropic and the energy equation can be expressed as

$$H_t=h+\frac{V^2}{2}=Constant \qquad \textbf{(21)}$$

We have

$$h_\infty+\frac{V_\infty}{2}=h+\frac{V}{2} \qquad \textbf{(22)}$$

We can use the isentropic relationships

$$h=C_pT \; ; \; C_p=\frac{\gamma R}{(\gamma-1)} \; ; \; a^2=\gamma RT \; ; \; M=\frac{V}{a} \qquad \textbf{(23)}$$

Substituting Eqns (23) into Eqn (22) and rearranging yields

$$a^2 = a_\infty^2 - \frac{\gamma-1}{2}(V^2 - V_\infty^2) \tag{24}$$

$$\frac{a^2}{a_\infty^2} = 1 - \frac{\gamma-1}{2}\left(\frac{V^2 - V_\infty^2}{V_\infty^2}\right) M_\infty^2 \tag{25}$$

Since the flow is 3 dimensional, we have

$$V^2 = u^2 + v^2 + w^2 \quad ; \quad V_\infty = U_\infty \tag{26}$$

Substituting in Eqns (18) and rearranging yields

$$V^2 - U_\infty^2 = 2U_\infty u' + u'^2 + v'^2 + w'^2 \tag{27}$$

Substituting Eqn (27) into Eqn (25) yields

$$\frac{a^2}{a_\infty^2} = 1 - \frac{\gamma-1}{2}\left(\frac{2U_\infty u' + u'^2 + v'^2 + w'^2}{U_\infty^2}\right) M_\infty^2 \tag{28}$$

Taking the reciprocal of Eqn (28)

$$\frac{a_\infty^2}{a^2} = \frac{1}{1 - \frac{\gamma-1}{2}\left(\frac{2U_\infty u' + u'^2 + v'^2 + w'^2}{U_\infty^2}\right) M_\infty^2} \tag{29}$$

Using the Binomial Expansion on Eqn (29)

$$\frac{a_\infty^2}{a^2} = 1 + \frac{\gamma-1}{2} M_\infty^2 \left(\frac{2U\infty u' + u'^2 + v'^2 + w'^2}{U_\infty^2}\right) + H.O.T. \tag{30}$$

From Eqn (20), the first term can be expanded as

$$\left(1 - \frac{u^2}{a^2}\right) = 1 - \left(\frac{U_\infty^2 + 2U_\infty + u'^2}{a^2}\right) \frac{U_\infty^2 a_\infty^2}{U_\infty^2 a_\infty^2} = 1 - \left(\frac{U_\infty^2 + 2U_\infty + u'^2}{U_\infty^2}\right) M_\infty^2 \frac{a_\infty^2}{a^2} \tag{31}$$

Substituting Eqn (30) into Eqn (31) yields

$$(1-\frac{u^2}{a^2}) = 1-(1+\frac{2u'}{U_\infty}+\frac{u'^2}{U_\infty^2})M_\infty^2[1+\frac{\gamma-1}{2}M_\infty^2(\frac{2u'}{U_\infty}+\frac{u'^2}{U_\infty^2}+\frac{v'^2}{U_\infty^2}+\frac{w'^2}{u_\infty^2})] \quad (32)$$

Eqn (32) can be simplified by neglecting the higher order terms (H.O.T.) to give

$$(1-\frac{u^2}{a^2}) = 1-M_\infty^2[1+\frac{2u'}{U_\infty}(1+\frac{\gamma-1}{2}M_\infty^2)] \quad (33)$$

Substituting Eqn (33) into Eqn (20) yields

$$[1-M_\infty^2-\frac{2u'}{U_\infty}M_\infty^2(1+\frac{\gamma-1}{2}M_\infty^2)]\frac{\partial u}{\partial x}+\frac{\partial v}{\partial y}+\frac{\partial w}{\partial z}=0 \quad (34)$$

Rearranging Eqn (34) yields

$$(1-M_\infty^2)\frac{\partial u}{\partial x}+\frac{\partial v}{\partial y}+\frac{\partial w}{\partial z}=\frac{2u'}{U_\infty}M_\infty^2(1+\frac{\gamma-1}{2}M_\infty^2)\frac{\partial u}{\partial x} \quad (35)$$

Rewriting Eqn (35) in terms of the perturbation velocities gives

$$(1-M_\infty^2)\frac{\partial(U_\infty+u')}{\partial x}+\frac{\partial v'}{\partial y}+\frac{\partial w'}{\partial z}=\frac{2u'}{U_\infty}M_\infty^2(1+\frac{\gamma-1}{2}M_\infty^2)\frac{\partial(U_\infty+u')}{\partial x} \quad (36)$$

We assume that

$$\frac{\partial U_\infty}{\partial x}=0 \quad (37)$$

Expanding Eqn (36), substituting into Eqn (37) and neglecting 2nd order perturbation terms yields

$$(1-M_\infty^2)\frac{\partial u'}{\partial x}+\frac{\partial v'}{\partial y}+\frac{\partial w'}{\partial z}=\frac{M_\infty^2}{U_\infty^2}(1+\frac{\gamma-1}{2}M_\infty^2)2u'\frac{\partial u'}{\partial x} \quad (38)$$

Since the flow is irrotational, we have

$$u' = \frac{\partial \phi}{\partial x} ; v' = \frac{\partial \phi}{\partial y} ; w' = \frac{\partial \phi}{\partial z} \qquad (39)$$

Substituting Eqn (39) into Eqn (38) gives the small perturbation potential equation for transonic flows

$$(1 - M_\infty^2)\phi_{xx} + \phi_{yy} + \phi_{zz} = \frac{M_\infty^2}{U_\infty^2}\left(1 + \frac{\gamma - 1}{2} M_\infty^2\right) 2\phi_x \phi_{xx} \qquad (40)$$

B. AN EXACT SOLUTION FOR AXI-SYMMETRIC BODIES IN TRANSONIC FLOW

Solutions to the two-dimensional, small perturbation potential equation for transonic flow have been accomplished by Biblarz [Ref. 4] by using the separation of variables approach. The solution of the small perturbation transonic flow equation has enabled the generation of shockless boundary surfaces. Al-Hashel [Ref. 5] reports on axi-symmetric boundary surfaces for M_∞=1.0, 1.10 and 1.20.

III. DRAG

Drag can be defined as the fluid dynamic force acting against an object placed in the stream of airflow. Basically, the drag force can be divided into two broad categories. The categories are viscous or skin friction drag and pressure drag.

Viscosity is the molecular "resistance" which fluid particles exhibit against displacement in relation to each other and with respect to the surface of solid objects. Such resistance presents itself in the form of frictional force, which is comparable to that of solid surfaces sliding along each other. This frictional force is a tangential force which occurs when a fluid (such as air) flows past a body. This force is the skin friction drag. At very low speeds or in flows associated with fluids of high viscosity and bodies of very small dimensions (i.e., at very low Reynolds number flow), viscosity is the predominant property determining the drag of a body [Ref. 6]. At higher Reynolds number flows, other forms of drag, such as turbulent skin friction drag, begins to have significant contribution.

In contrast to the skin friction drag (which is a tangential force), pressure drag results from the distribution of pressure forces normal to the body surface. Within the subsonic range of speeds, inviscid fluid dynamic theory predicts that the flow will close in behind an object, without any losses. Positive pressures at the front of the object are counterbalanced by the negative pressure of equal magnitude on the rear, resulting in the pressure drag being zero. This phenomenon is known as D'Alembert's Paradox. In real flows, however, such a phenomenon does not exist. The pressure at the rear side of an object can be very much lower than predicted from non-viscous flow conditions. Viscosity causes the formation of a boundary layer which may cause flow separation

on the surface of an object. The resultant pressure differential between the pressures on the forward side and the lower pressures on the rear side represents the pressure drag. In blunt or bluff bodies, this type of drag is usually much higher than the skin friction drag [Ref. 6]. For streamlined or aerodynamically shaped bodies, the reverse is true. For flow in the transonic regime, the formation of shocks contributes to the pressure drag due to the pressure differential between the forward portion of an object and the rear portion of the object. Figure (3.1) [Ref. 7] shows the typical drag composition of an axi-symmetric projectile shaped body. Figure (3.2) [Ref. 8] shows the variation in skin friction drag and wave drag as a function of free-stream Mach number for a body of revolution at zero incidence.

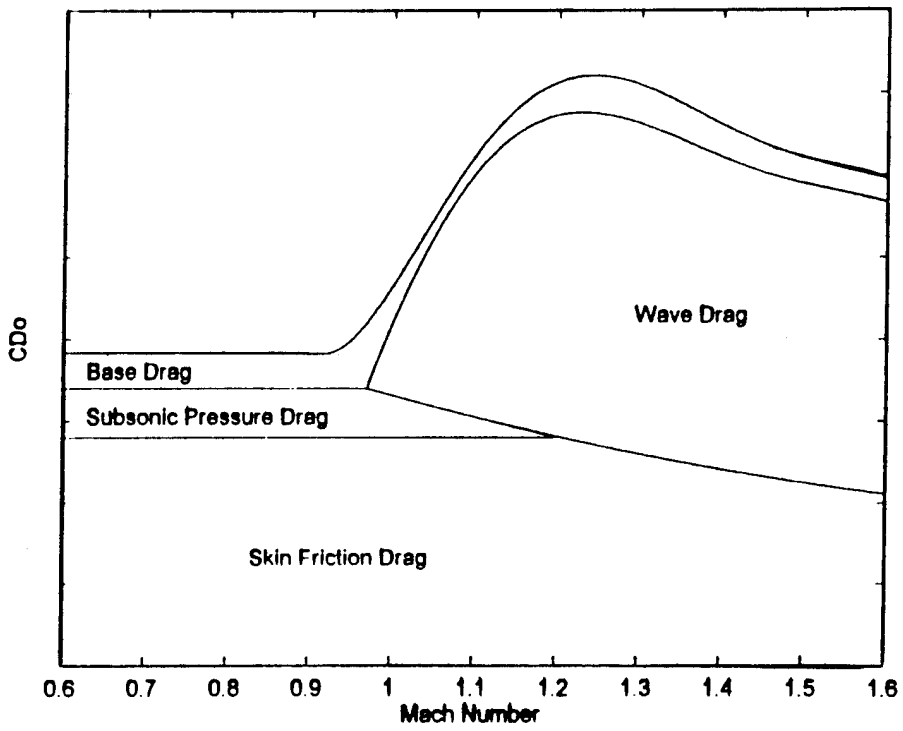

Figure 3.1. Components of Drag [Ref. 7]

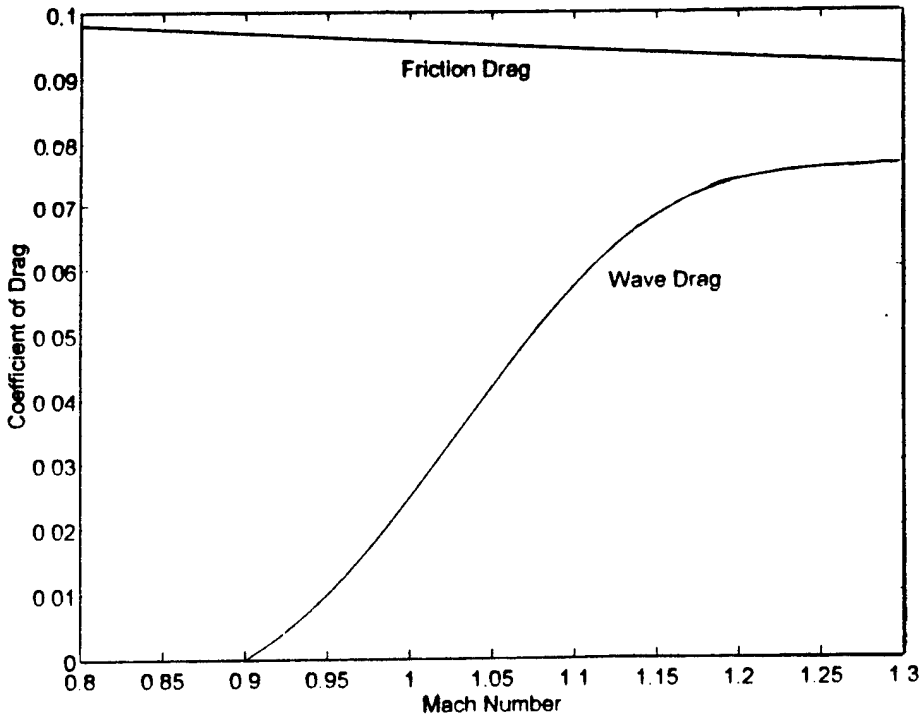

Figure 3.2. Friction and Wave Drag Variation [Ref. 8]

One well-known method of reducing the drag on an axi-symmetric body is by streamlining the afterbody, i.e., reducing its base diameter gradually. Figure (3.3) [Ref. 6] shows the reduction in zero incidence drag coefficient for boat-tailed afterbodies. Other approaches of reducing drag on a streamlined body includes mechanical methods such as vortex generators and methods for controlling the boundary layer such as the boundary layer suction method.

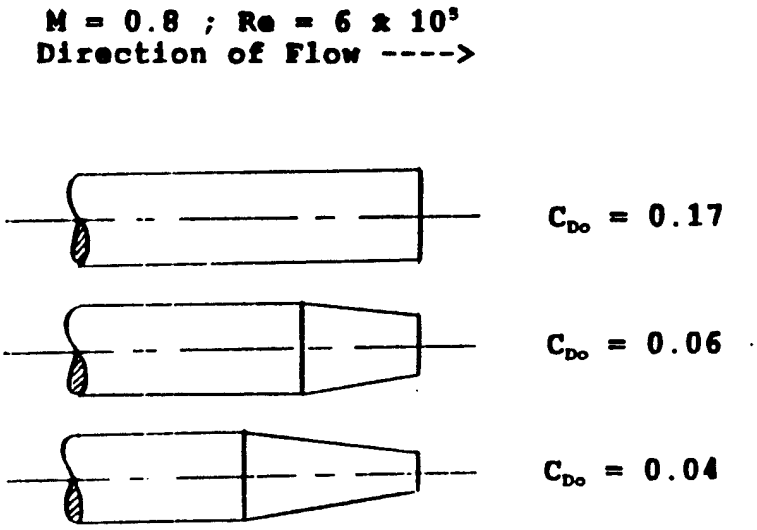

Figure 3.3. Drag Coefficient of Boat-Tailed Afterbodies [Ref. 6]

Numerous methods are available to calculate the theoretical values of drag on an object. However, there are no totally satisfactory method of accurately calculating viscous drag, particularly transonic drag. This is due in large to the necessary assumptions and simplifications to the full Navier-Stokes equations to facilitate mathematical solutions and the need to use turbulence models for the boundary layer effects in high Reynolds Number flows. In this work, both the skin friction drag and the pressure drag can be obtained directly from the results of CFD computations [Ref. 3].

IV. COMPUTATIONAL FLUID DYNAMICS (CFD)

Rapid advancement in the speed and efficiency of computing and better modellings has led to the emergence of computational fluid dynamics as an important branch of aerodynamics. CFD complements the experimental and theoretical branches of fluid dynamics by providing a relatively accurate and cost-effective means of simulating real flows. Another significant advantage of CFD is the convenience of being able to vary any relevant parameter of the flow and also the ability to "switch off" specific terms in the governing equations so as to assist the researcher in understanding their contributions to the resultant flow.

In this work, CFD was used to compute the axi-symmetric flow over complete body models which are composed of a forebody (ellipsoid) and an afterbody (conical or special shape) using a Navier-Stokes flow-solver. The surface profile of the special shape afterbody was reported on by Al-Hashel [Ref. 5] using an exact solution method for small perturbation. The conical afterbody has a base diameter ratio (d_b/d_m) of 0.75 and a conical turning angle (β) of 14 degrees. A generic forebody in the shape of an ellipsoid was patched onto the afterbodies to establish the CFD working models.

A. GRID GENERATION

A computational grid system is a necessary part of any numerical solution based on a finite-difference or finite-element method. The selection of a grid system is based primarily on the requirement for accuracy in the final solution. Secondary considerations are the effects on computational efficiency of the solution algorithm using available computer architecture and, finally, the ease of grid generation.

The grids for the two models used were generated by Priyono [Ref. 9] using the computer programs GRAPE [Ref. 10] and GRIDGEN2D [Ref. 11]. These programs were used to generate two-dimensional grids which were subsequently converted into 3-D grids utilizing the FORTRAN codes d2d3.f and rotategr.f [Appendix B]. GRAPE was used to generate the grid for the model with the special shape afterbody (model CNTR11). GRIDGEN2D was used to generate the grid for the model with the conical afterbody (model CBXCN2), since GRAPE cannot accomodate the non-smooth points associated with the conical afterbody. The grids for the two models are shown at Figures (1) and (2) in Appendix A. In this work, the correspondence between the two body profiles was verified prior to further analysis. This correspondence is shown in Figure (3) in Appendix A.

Since the analysis was for the complete body, an O-type grid was used. Previous work by Priyono demonstrated the need to use a fine grid due to the significant propagation of the bow shock above and below the body in transonic flow, especially in the vicinity of freestream Mach number of unity. It was necessary for the bow shock to diminish before it reached the grid boundary, thereby ensuring that the shock is not reflected by the grid boundary and contaminated the solution. The outer boundary of the fine grid was 5 times the body's length. The grids were generated only for half of the complete body taking advantage of symmetry. The grid size used is 77x15x120.

B. FLOW-SOLVER

The OVERFLOW program was developed by NASA Ames Research Center. The version used is Version 1.6ag released on 30 April 1993 [Ref. 3]. The program uses either the 3-D Euler or Navier-Stokes flow-solvers for inviscid or viscous flow computations respectively. The selection of Euler or Navier-

Stokes flow-solver is accomplished by setting the parameter VISINP (viscosity input) to True or False in the input file.

Before applying the flow-solver code (OVERFLOW), the formatted 3-D grid file (grid.for) must be converted into an unformatted input grid file (grid.in). This is accomplished using the FORTRAN code readx.f [Appendix B]. An input file (overflow.in) containing all the input parameters must then be written for running OVERFLOW. The input parameters consist of the number of iterations, timesteps, calculation methods, smoothing method, types of in-flow and out-flow, boundary conditions and types of turbulence models. The value of angle of attack (ALPHA) depends on the orientation of the grid in the coordinate system. In our case, ALPHA was set at 180° (i.e., flow comes from the x-positive to the x-negative direction). A typical input file (overflow.in) is provided in Appendix B.

In his work, Priyono investigated the flow past afterbodies only using both the Euler and Navier-Stokes flow-solvers. Priyono also investigated the flow past complete bodies but only with the Euler flow-solver. For the present work which investigates the flow past complete bodies using the Navier-Stokes flow-solver, the effects of viscosity have to be "switched on". This is accomplished by setting VISCJ, VISCK and VISCL parameters to TRUE. This in effect includes viscous terms into the J (along the body in the x-direction), K (around the body or x-axis) and L (outwards from the body towards the outer grid boundary) computational directions. The number of turbulent wall regions NTURB is set to 2. This corresponds to the turbulence models ITTYP of 1 and 11, i.e., the Baldwin-Lomax boundary layer model (with variable Degani-Schiff cutoff) for the body in general and the Baldwin-Lomax shear layer model (with variable C_{wk}) to model the wake behind the body. The basis of selecting the turbulence models comes from the OVERFLOW manual which recommends the use of the

Baldwin-Lomax model for flows with mild separation.

The OVERFLOW program generates output files such as overflow.out, fomo.out, rpmin.out, resid.out and q.save. The file overflow.out provides information on the input parameters which are used in the computational run. The file fomo.out provides the force and moment history, which in this case, includes coefficients of drag due to pressure (which was also computed when using the Euler flow solver) and viscosity (i.e., skin friction drag). The file rpmin.out provides the minimum density/pressure/ratio of specific heats history. The file resid.out provides flow solver residual history for the five primary variables (i.e., ρ, ρu, ρv, ρw and e, where e is the total energy). The variable that is used to show convergence of the solution is the density residual. In general, the convergence criterion can be defined as the reduction in the density residuals by two orders of magnitude and the trend towards further reduction. The file q.save is the solution file in PLOT3D format [Ref. 12] when OVERFLOW has run satisfactorily. If the flow-solver detects a case of negative density or pressure during the computation process, an output file called q.bomb will be generated instead of the solution output file q.save. The file q.bomb thus represents the solution prior to the error being detected.

The output from resid.out is a text file and the result can be plotted using a plotting software such as GNUPLOT [Ref. 13]. The output from fomo.out is also a text file and the values of coefficient of drag due to pressure and viscosity can be read off directly at the end of the file. The coefficient of drag can also be plotted using GNUPLOT to show convergence to a particular value. The output from q.save is an unformated file which needs to be converted into a formatted file (q.form) using the FORTRAN code readq.f [Appendix B]. The formatted solution file q.form can be plotted using either PLOT3D or FAST [Ref. 14]. Both software

packages are capable of generating plots showing the Mach number distribution, shock locations due to pressure difference, velocity vector distribution and many other options of flow visualization over the bodies. In this work, PLOT3D was used for all the flow visualization plots.

C. CFD SOLUTIONS

Initial turbulent flow computations were accomplished with the setting of ITDIR of 3 and 1, corresponding to the L and J coordinate directions away from the wall or shear layer for the Baldwin-Lomax boundary layer model and the Baldwin-Lomax shear layer model respectively. Solutions obtained from the computations displayed an asymmetry at the wake of the bodies. Logically, there should be no asymmetry since the computations were for zero incidence flow.

Re-examination of the input for ITDIR strongly indicated that the parameter should be set to 3 and 3, corresponding to the coordinate direction of L for both the turbulence models. Subsequent computations with this setting produced symmetry at the wake. The output also displayed a clear momentum deficit within the wake region aft of the bodies.

Having resolved the parameters for the turbulence modelling, the next step was to ensure effective convergence of the solutions. A slow start was used with DT = 0.01 and CFLMIN = 3.0 for all the runs. After 2000 iterations, it was observed that the density residuals were only converging to approximately 1.5 orders of magnitude. Since the viscous solution includes skin friction drag, the residual would have to show at least 2 orders of magnitude of convergence. In order to increase the convergence rate, the runs were initiated for either 500 or 1000 iterations with a CFLMIN = 3, depending on the free-stream Mach number. Subsequently, restarts were used and the values of CFLMIN or DT were varied. Typical variations of CFLMIN and DT are tabulated at Table (1)

in Appendix C. Figures (4) and (5) in Appendix A show typical plots for density residuals. The fluctuations in the residuals are caused by the effects of turbulence modelling.

The critical free-stream Mach number for both bodies was computed to be approximately past 0.8. This is in contrast to the Euler results reported by Priyono which show the inviscid critical Mach number as approximately 0.7 and that sonic conditions were reached in the regions where the forebody and afterbodies mate with the mid-sections. Figures (6) and (7) in Appendix A shows the Mach contours for CNTR11 and CBXCN2 respectively at M_∞=0.8 and the highest local Mach number displayed is 0.9, indicating that the critical Mach number has not been reached. Figures (8) and (9) in Appendix A shows the Mach contours and shock locations for CNTR11 at M_∞=0.95 respectively. Comparing Figure (9) with Figure (10) in Appendix A, which shows the shock locations for CBXCN2 at M_∞=0.95, note that the rear shock is further back at the aft portion of CNTR11. The viscous critical Mach number was higher due to the presence of the boundary layer which lessened the acceleration of the airflow over the forebody and also had a "rounding" effect on the afterbodies which translates into a slower acceleration around the aft regions.

Since this work uses the Navier-Stokes flow-solver, it is important to verify that the resultant flow is indeed a viscous solution. The plot at Figure (11) in Appendix A shows the velocity vector distribution over CNTR11 at a free-stream Mach number of 1.2. It is important to note the distinct boundary layer in the plot. It was also necessary to validate the no-slip condition on the surface of the bodies. The appropriate input parameters were used in PLOT3D to show only the Mach contours on the surface of the bodies. The results show a Mach contour of zero on the surface of the bodies, thereby confirming the no-slip condition.

The plots showing the shock locations based on pressure gradient complement the plots of Mach number distribution. The plots at Figures (12) and (13) in Appendix A for CNTR11 and CBXCN2 respectively at M_∞=1.05 show that a bow shock has formed once the free-stream Mach number goes supersonic. It is interesting to note that the plot at Figure (10) in Appendix A for free-stream Mach number of 0.95 corresponds to a schlieren picture at Figure (14) in Appendix A of a similar flow over an axi-symmetric body at free-stream Mach number of 0.95 at zero incidence [Ref. 15].

V. RESULTS, CONCLUSIONS AND RECOMMENDATIONS

A. RESULTS

The values of drag coefficient are obtained directly from the OVERFLOW output files fomo.out. The output from these files is plotted to show that the values of pressure drag coefficient and skin-friction drag coefficient are converged. A typical plot is shown at Figure (5.1). The viscous drag coefficients of the two bodies at the various Mach numbers are compared in Figure (5.2). The corresponding inviscid drag coefficients as computed by Priyono are indicated in Figure (5.3).

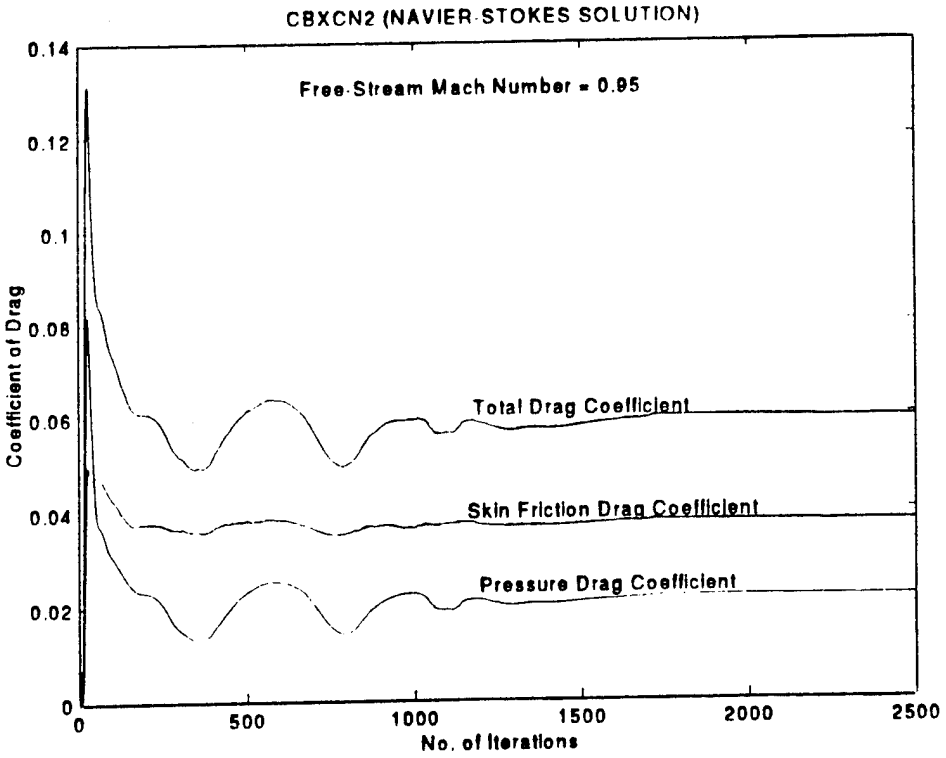

Figure 5.1. Convergence of Drag Coefficient

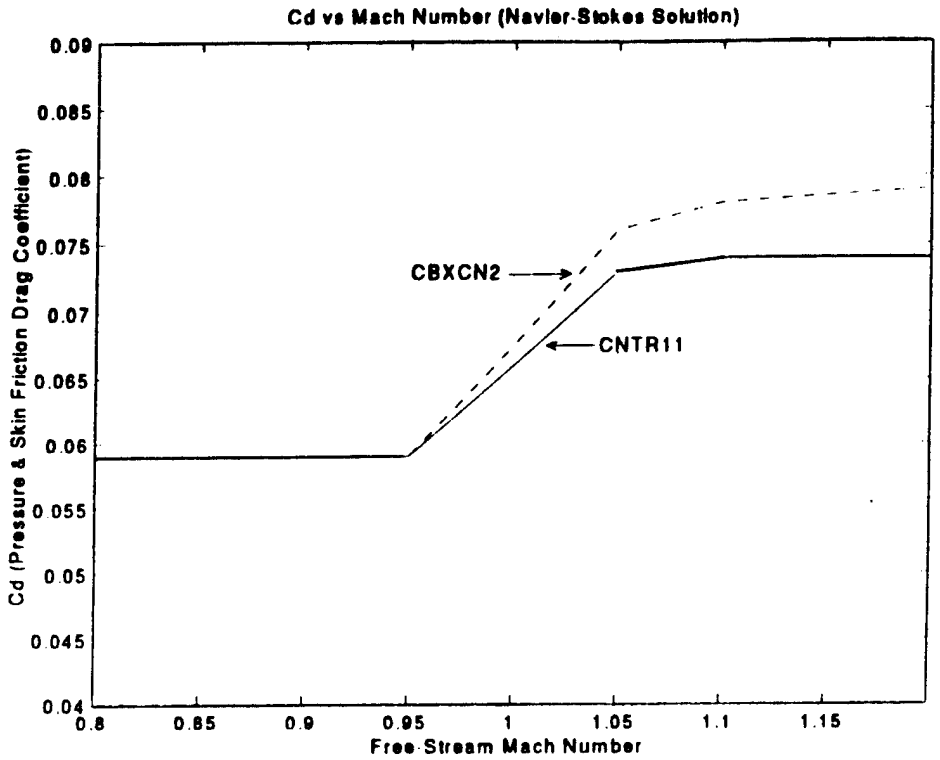

Figure 5.2. Drag Coefficient For Navier-Stokes Solutions

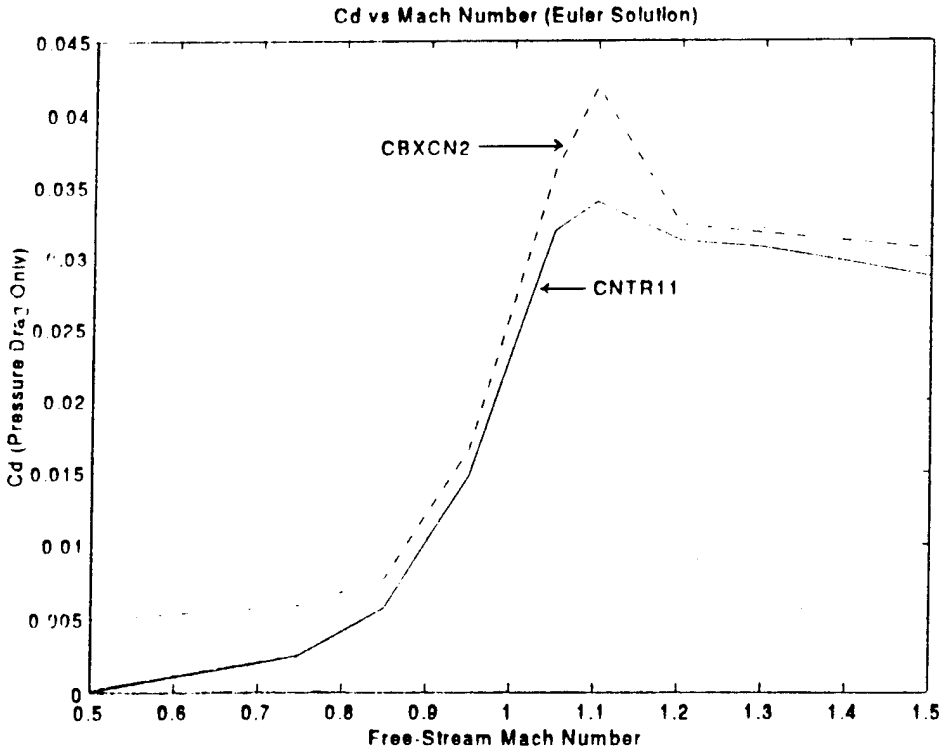

Figure 5.3. Drag Coefficient For Euler Solutions [Ref. 9]

As expected, the viscous drag coefficients are higher than the inviscid drag coefficients. These results show that skin friction drag coefficients are significant for the viscous solutions. The viscous solutions show a maximum drag coefficient difference of approximately 5.5% between the two bodies. In comparison, the Priyono [Ref. 9] reported a maximum drag coefficient difference of approximately 15% between the two bodies for the Euler solutions. The likely difference between these is the smoothing of the afterbody by the boundary layers.

The pressure drag coefficient remains relatively constant from the sub-sonic free-stream Mach number regime up until the critical Mach number. Subsequently, the pressure drag increases due to the addition of wave drag resulting from the formation of shock waves. The skin friction drag coefficient, on the other hand, decreases with increasing free-stream Mach number. The drag coefficients as shown in Figure (5.2) is in good agreement with typical values as shown in Figures (3.1) and (3.2). Preliminary results for free-stream Mach numbers of 1.3 and 1.5 show that the drag coefficient decreases from the peak value shown at Figure (5.2).

The results show that the special shape afterbody did indeed provide a lower drag coefficient as compared to the conical afterbody. The plots from shock location for free-stream Mach number of 0.95 clearly shows the position of the rear shock wave as being further aft of the special shape afterbody when compared with the rear shock wave location for CBXCN2.

B. CONCLUSIONS AND RECOMMENDATIONS

The OVERFLOW code has proven to be a useful CFD tool for this work. In hindsight, it would have been preferable to generate the grids for both the bodies using one grid generation method instead of using GRAPE for CNTR11 and

GRIDGEN2D for CBXCN2. The advantage would have been complete commonality between the grids for the two bodies with the only variations being at the aft portions. As mentioned earlier, although the profile of the two bodies were verified, the positioning of the grid points on the two bodies (especially on the forebody) were different. This difference may affect the accuracy of the solutions.

The investigation of the two axi-symmetric bodies using CFD has shown an advantage of the special shaped afterbody in the form of lower transonic viscous drag coefficient over the conical shaped afterbody by a maximum difference of approximately 5.5%. This advantage is over and above the benefits that one can achieve by boat-tailing the afterbody as shown in Figure (3.3). These results can be used to design low pressure drag surfaces for shapes such as missiles, projectiles, aircraft external ferry tanks and aircraft engine nacelles for improved performance within the transonic flight regime.

Finally, this work may be continued with experimental validation of the advantage of the special shaped afterbody over the simple conical afterbody using an appropriate transonic wind-tunnel. Further CFD work could also be carried out to investigate the effects of angle-of-attack on the two bodies. Such efforts would contribute useful experimental data on the transonic flow regime, the likes of which is certainly lacking currently.

LIST OF REFERENCES

1. Nixon, D., "Transonic Aerodynamics", AIAA, Progress in Astronautics and Aeronautics, Vol. 81, 1982.

2. Bertin, J.J., and Smith, M.L., "Aerodynamics for Engineers", Prentice Hall, 1989.

3. Buning, P.G., and others, "Overflow User's Manual Version 1.6ag", NASA Ames Research Center, California, April, 1993.

4. Biblarz, O., "An Exact Solution to the Transonic Equation", Israel Journal of Technology, Vol. 13, 1975.

5. Al-Hashel, W.I., "Two-Dimensional Boundary Surfaces for Axi-Symmetric External Transonic Flows", Master's Thesis, Naval Postgraduate School, Monterey, CA, 1993.

6. Hoerner, S.F., "Fluid Dynamic Drag", Hoerner Publication, 1965.

7. Hoak, D.E., and Finck, R.D., "USAF Stability and Control DATCOM", Flight Control Division, Airforce Flight Dynamics Laboratory, Wright-Patterson AFB, Ohio, 1978.

8. Moulden, T.H., "Fundamentals of Transonic Flow", John Wiley and Sons, Inc., 1984.

9. Priyono, E., "An Investigation of the Transonic Pressure Drag Coefficient for Axi-Symmetric Bodies", Master's Thesis, Naval Postgraduate School, Monterey, CA, 1994.

10. Sorenson, R.L., "A Computer Program to Generate Two-Dimensional Grids About Airfoils and Other Shapes by the use of Poison's Equation", NASA Technical Memorandum 81198, 1981.

11. Steinbrenner, J.P., Chawner, J.R., "The Gridgen V.8 Multiple Block Grid Generation Software", MDA Engineering, Inc., Arlington, Texas, December 1992.

12. Walatka P.P., Buning P.G., "PLOT3D User's Manual Version 3.5", NASA Ames Research Center, California, 1989

13. Williams T., Kelley C., "GNUPLOT - An Iterative Plotting Program Version 3.4", 1993.

14. "Flow Analysis Software Toolkit Version 1.1a - FAST", Numerical Aerodynamics Simulation (NAS) Division, NASA Ames Research Center.

15. Van Dyke, M., "An Album of Fluid Motion", The Parabolic Press, 1982.

APPENDIX A. CFD RESULTS

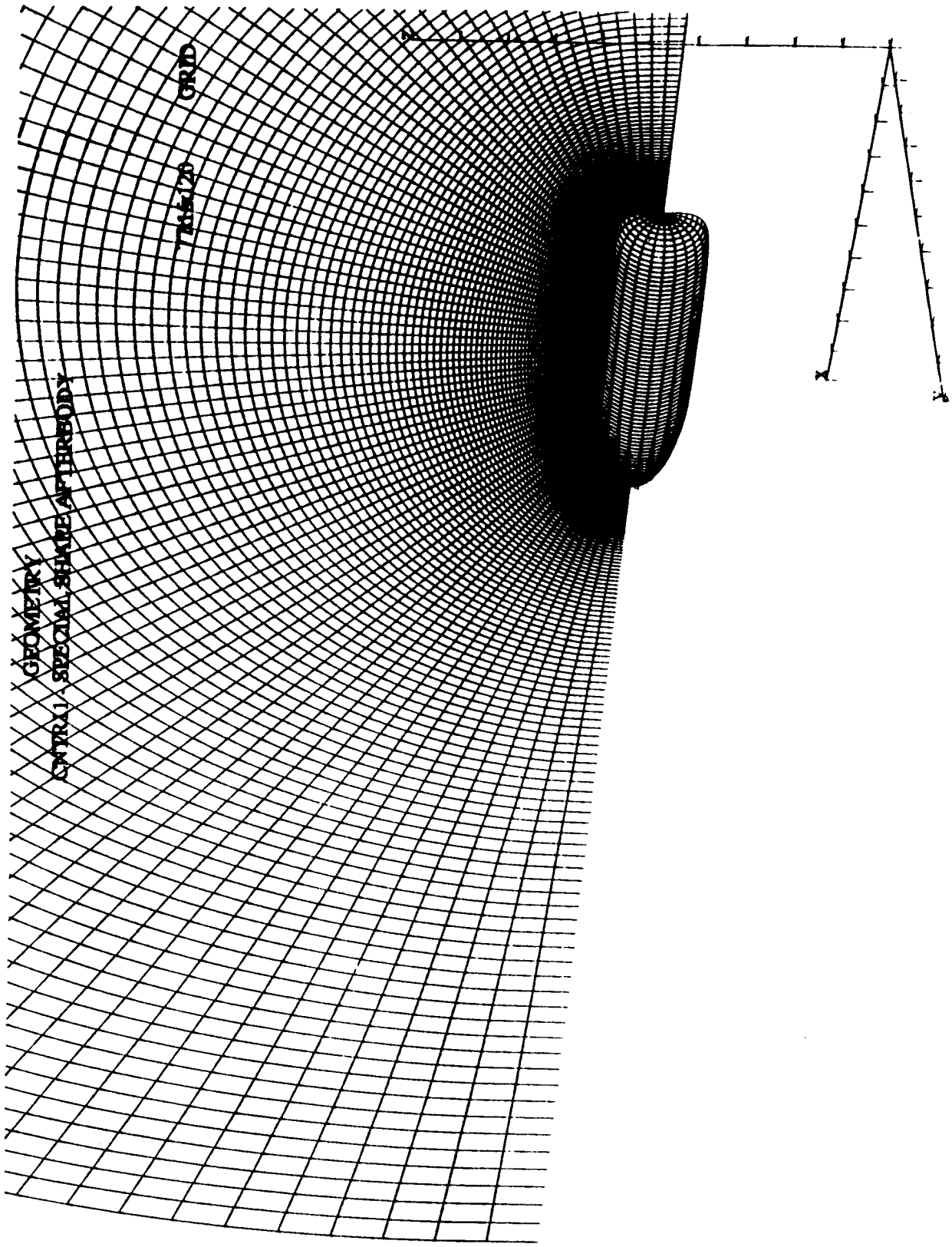

Figure 1

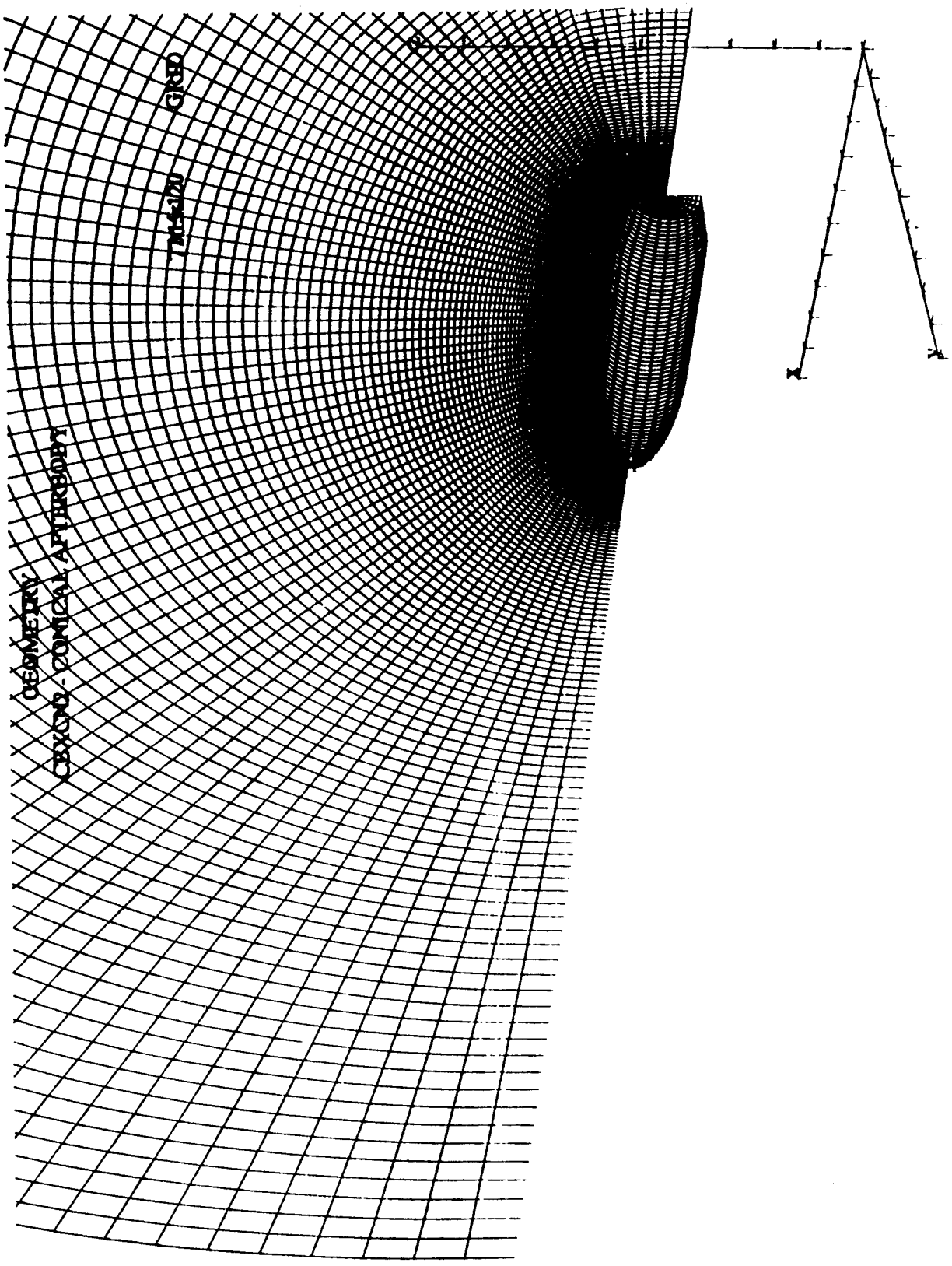

Figure 2

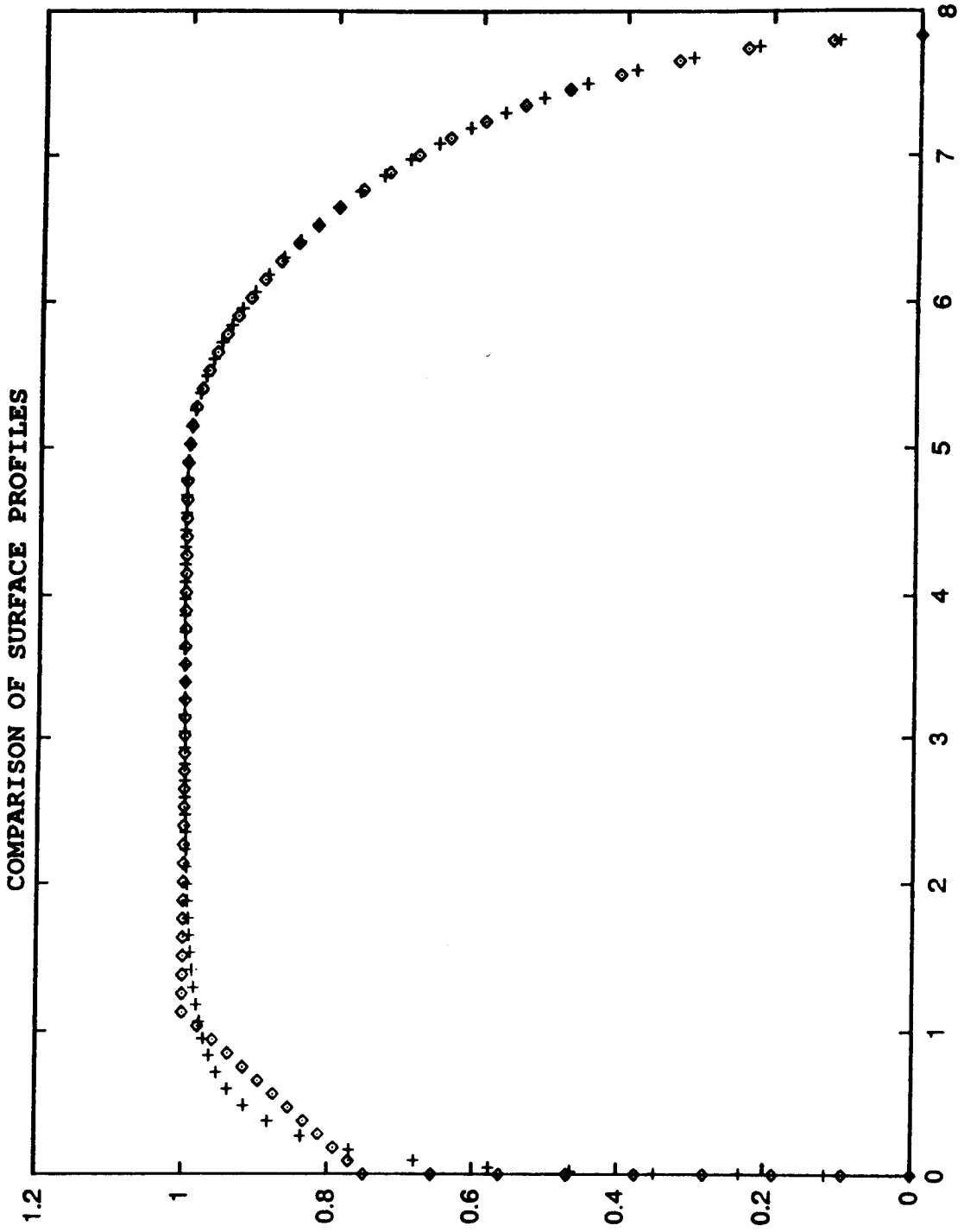

Figure 3

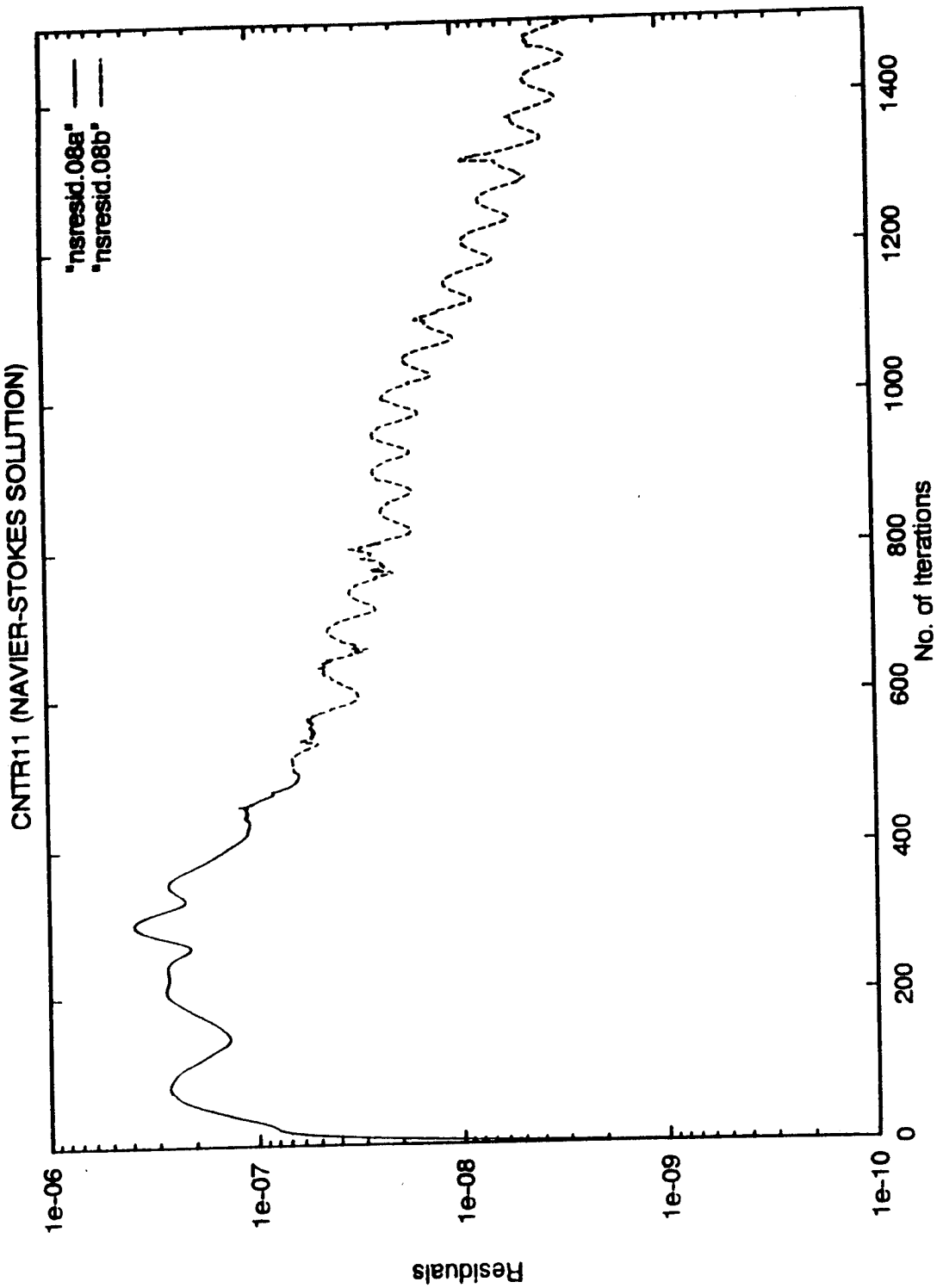
CNTR11 (NAVIER-STOKES SOLUTION)
"nsresid.08a"
"nsresid.08b"
Residuals
1e-06
1e-07
1e-08
1e-09
1e-10
0
200
400
600
800
1000
1200
1400
No. of Iterations

Figure 4

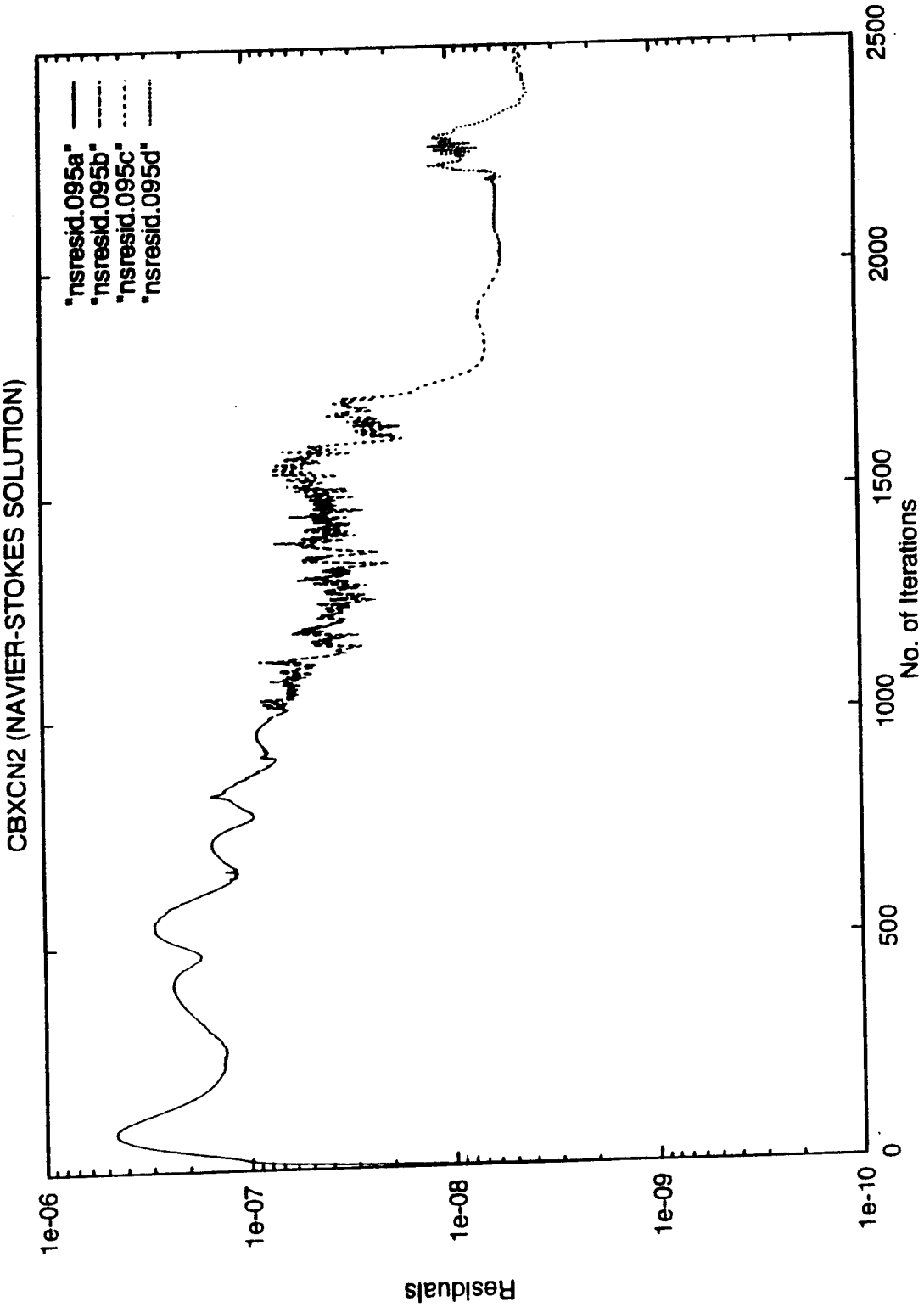
CBXCN2 (NAVIER-STOKES SOLUTION)
"nsresid.095a"
"nsresid.095b"
"nsresid.095c"
"nsresid.095d"
Residuals
1e-06
1e-07
1e-08
1e-09
1e-10
0
500
1000
1500
2000
2500
No. of Iterations

Figure 5

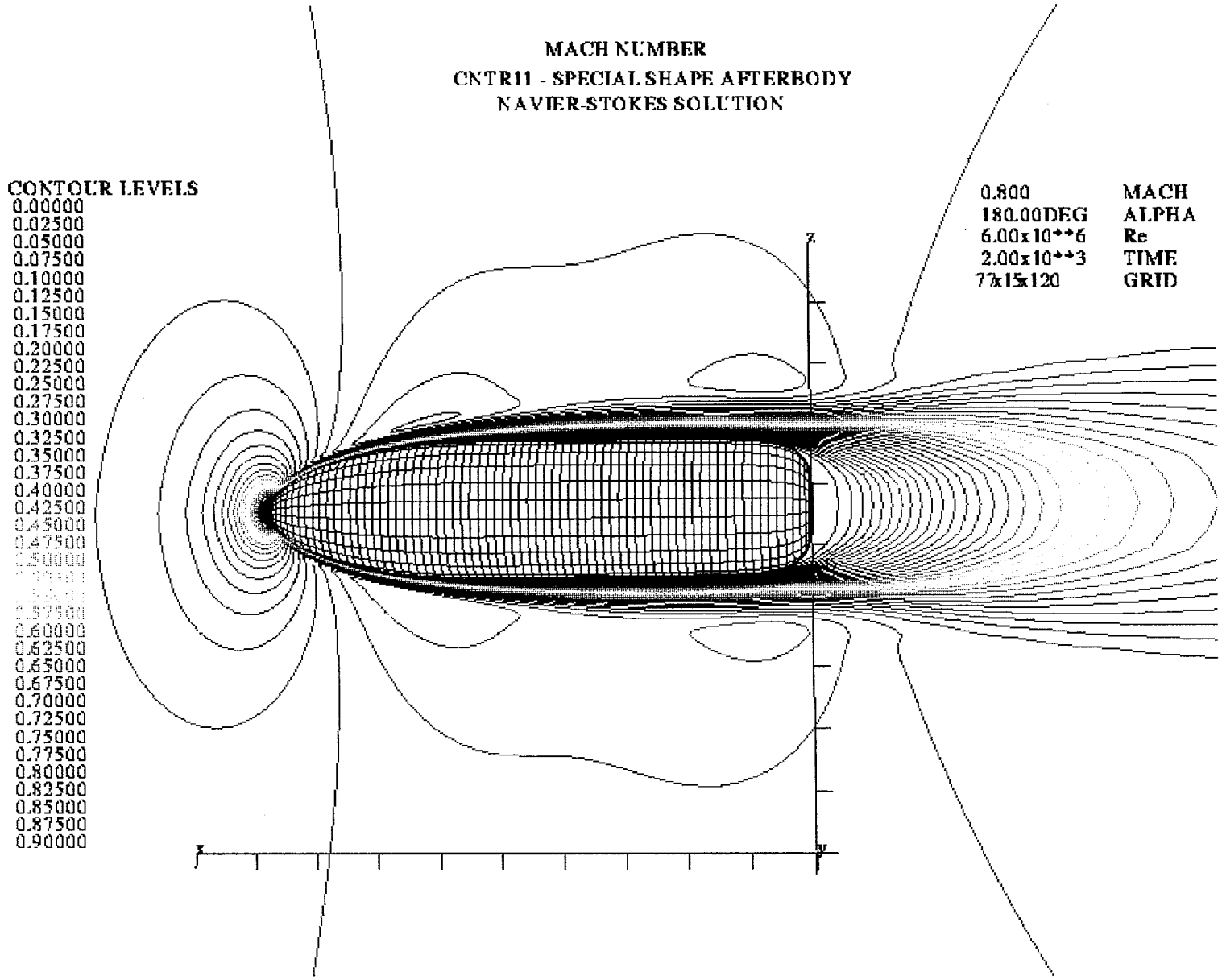
MACH NUMBER
CNTR11 - SPECIAL SHAPE AFTERBODY
NAVIER-STOKES SOLUTION
CONTOUR LEVELS
0.00000
0.02500
0.05000
0.07500
0.10000
0.12500
0.15000
0.17500
0.20000
0.22500
0.25000
0.27500
0.30000
0.32500
0.35000
0.37500
0.40000
0.42500
0.45000
0.47500
0.60000
0.62500
0.65000
0.67500
0.70000
0.72500
0.75000
0.77500
0.80000
0.82500
0.85000
0.87500
0.90000
0.800 MACH
180.00DEG ALPHA
6.00x10**6 Re
2.00x10**3 TIME
77x15x120 GRID
Z
X
Y

Figure 6

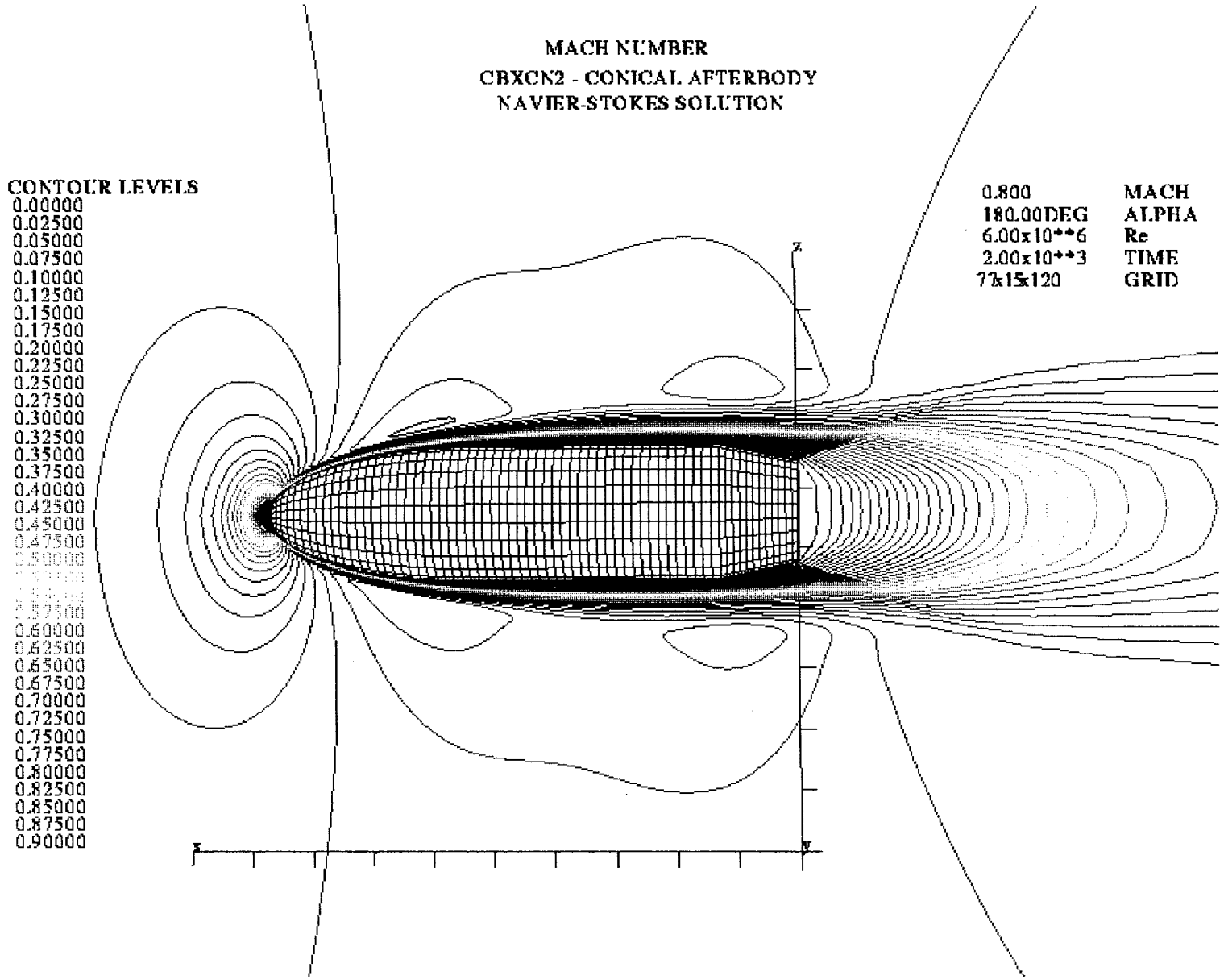
MACH NUMBER
CBXCN2 - CONICAL AFTERBODY
NAVIER-STOKES SOLUTION
CONTOUR LEVELS
0.00000
0.02500
0.05000
0.07500
0.10000
0.12500
0.15000
0.17500
0.20000
0.22500
0.25000
0.27500
0.30000
0.32500
0.35000
0.37500
0.40000
0.42500
0.45000
0.47500
0.60000
0.62500
0.65000
0.67500
0.70000
0.72500
0.75000
0.77500
0.80000
0.82500
0.85000
0.87500
0.90000
0.800 MACH
180.00DEG ALPHA
6.00x10**6 Re
2.00x10**3 TIME
77x15x120 GRID
Z
X
Y

Figure 7

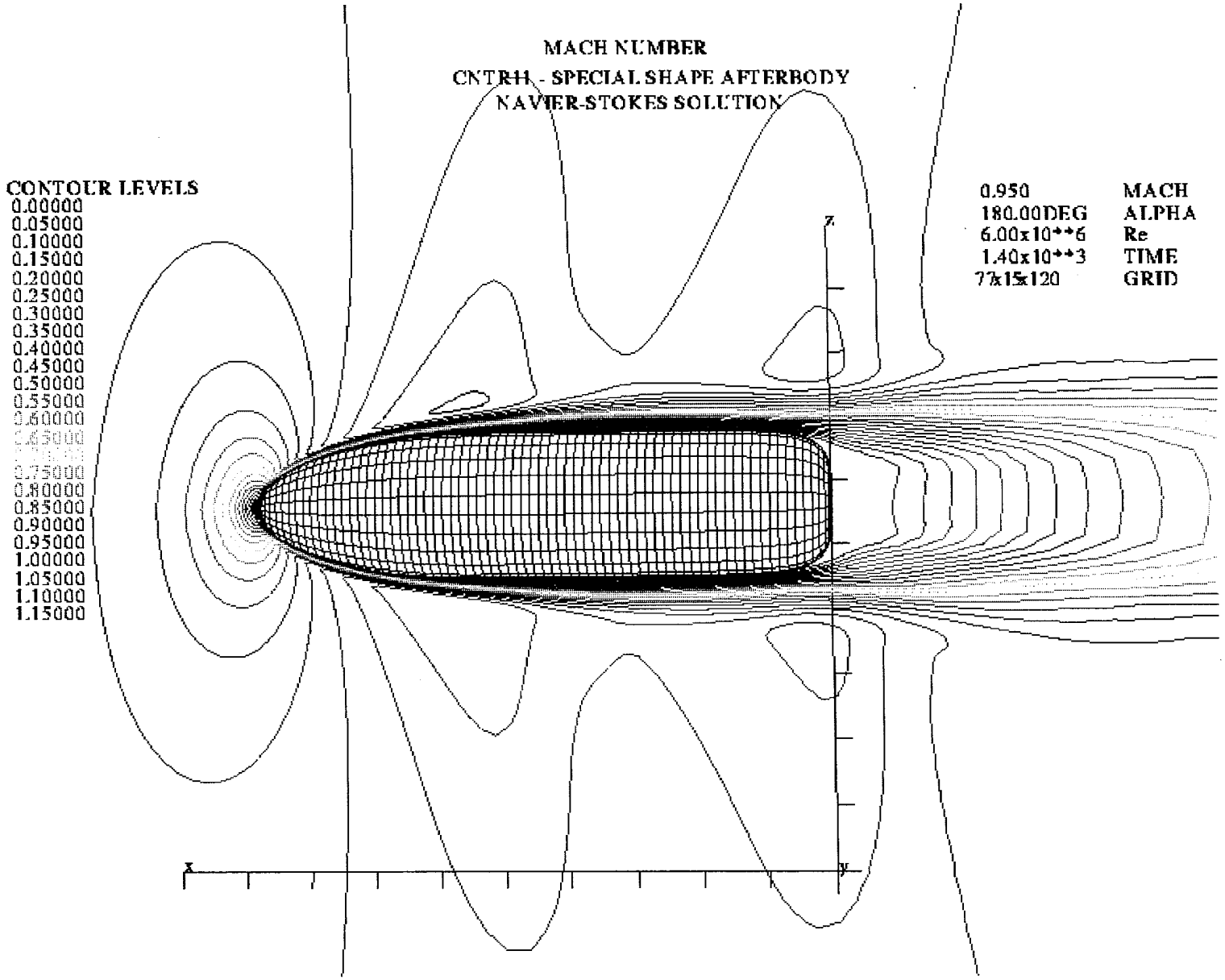
MACH NUMBER
CNTR11 - SPECIAL SHAPE AFTERBODY
NAVIER-STOKES SOLUTION
CONTOUR LEVELS
0.00000
0.05000
0.10000
0.15000
0.20000
0.25000
0.30000
0.35000
0.40000
0.45000
0.50000
0.55000
0.60000
0.75000
0.80000
0.85000
0.90000
0.95000
1.00000
1.05000
1.10000
1.15000
0.950 MACH
180.00DEG ALPHA
6.00x10**6 Re
1.40x10**3 TIME
77x15x120 GRID
Z
X
Y

Figure 8

SHOCK LOCATIONS BASED ON PRESSURE GRADIENT
CNTR11 - SPECIAL SHAPE AFTERBODY
NAVIER-STOKES SOLUTION

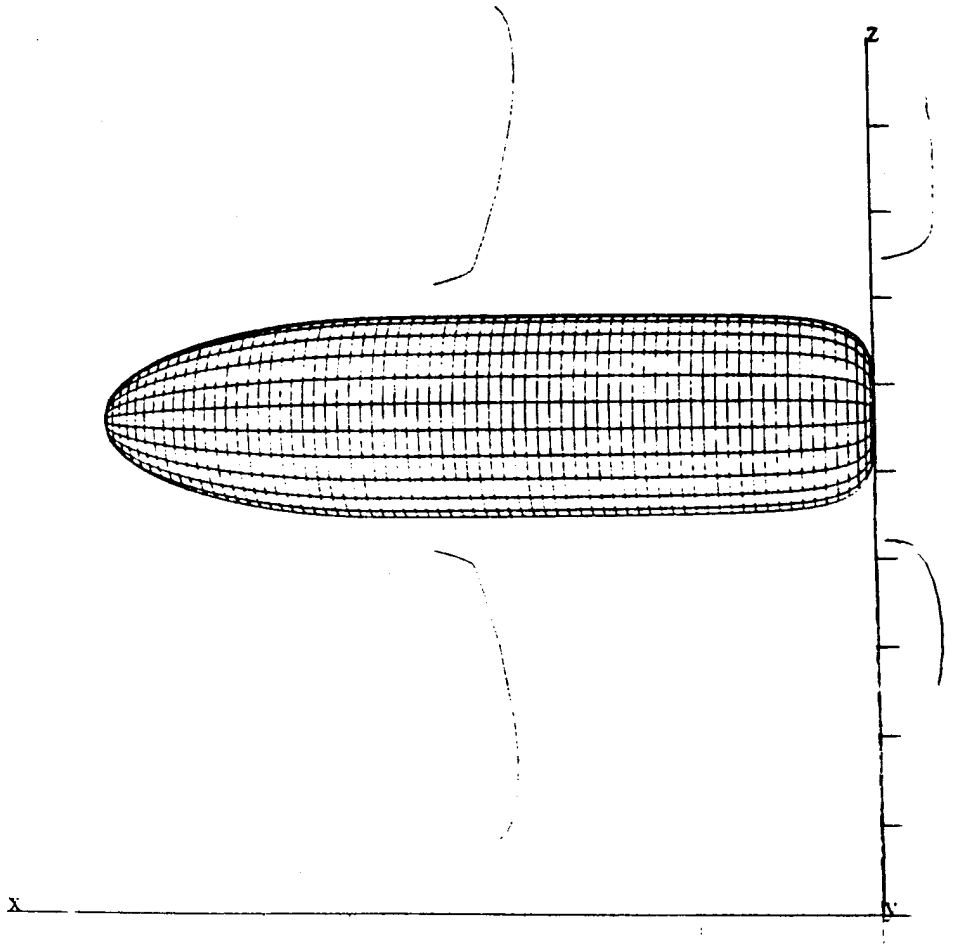

0.950	MACH
180.00DEG	ALPHA
6.00x10**6	Re
1.40x10**3	TIME
77x15x120	GRID

Figure 9

SHOCK LOCATIONS BASED ON PRESSURE GRADIENT
CBXCN2 - CONICAL AFTERBODY
NAVIER-STOKES SOLUTION

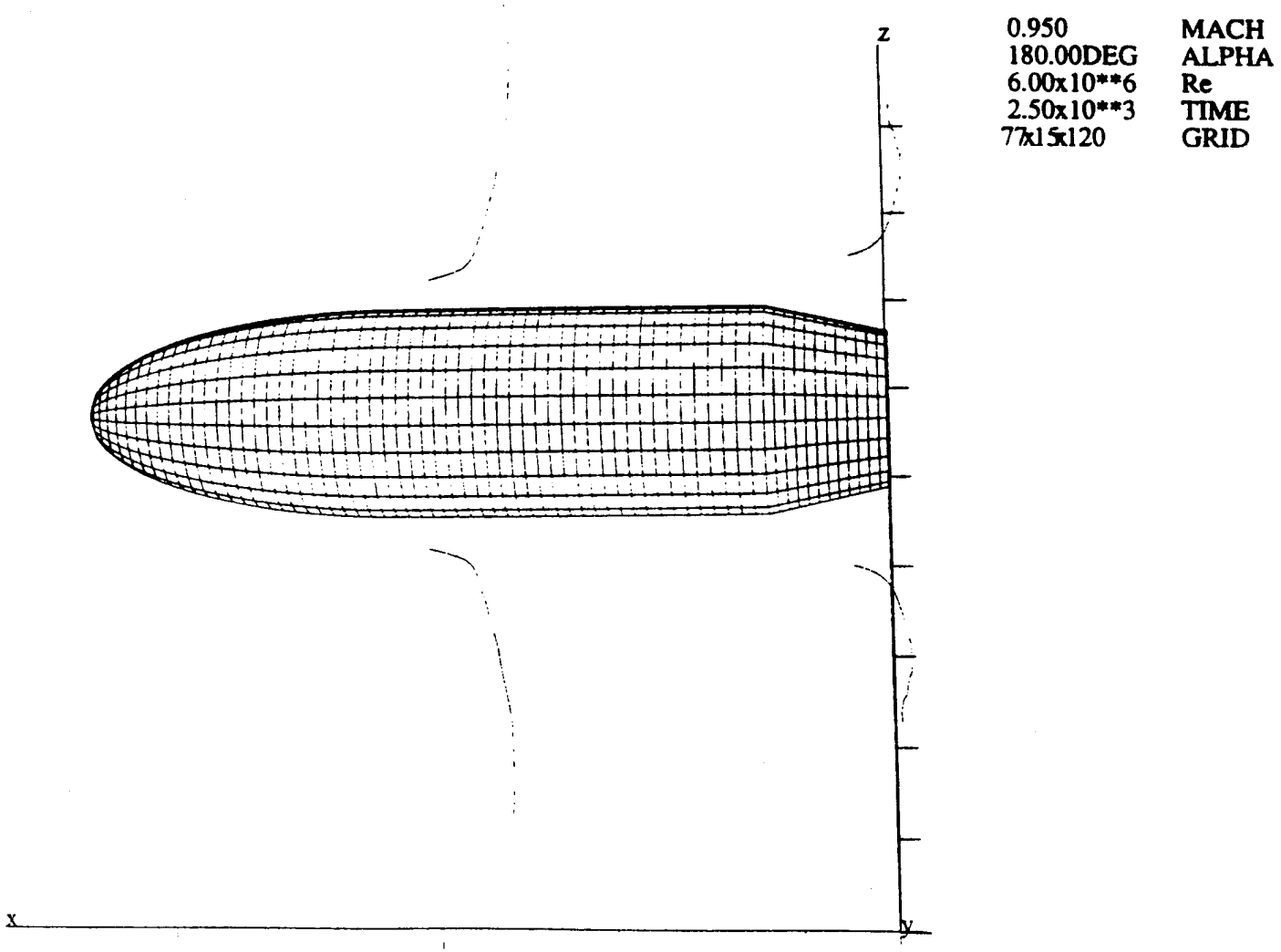

Figure 10

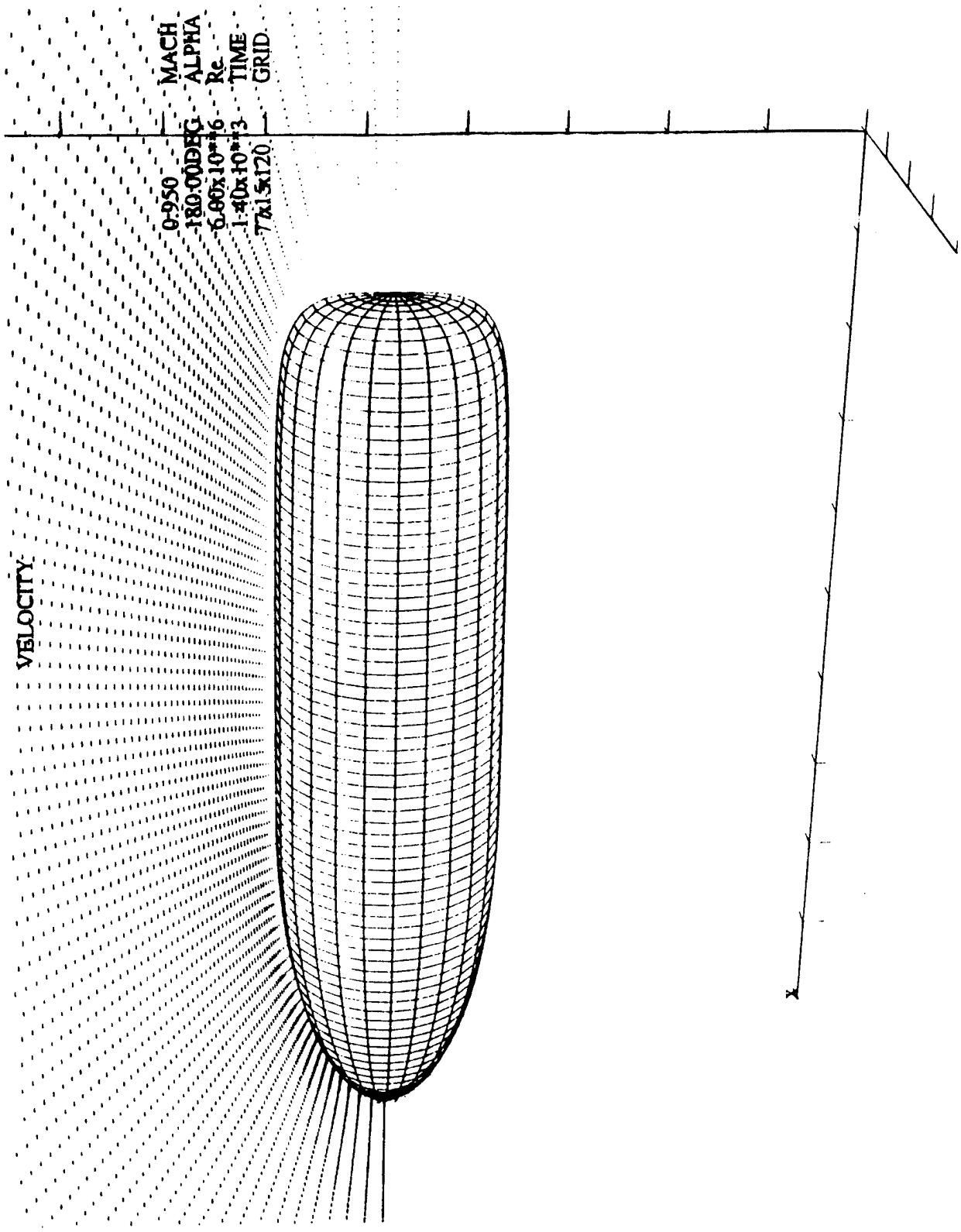
MACH
ALPHA
Re
TIME
GRID
0.950
180.00DEG
6.00x10**6
1.40x10**3
77x15x120
VELOCITY

Figure 11

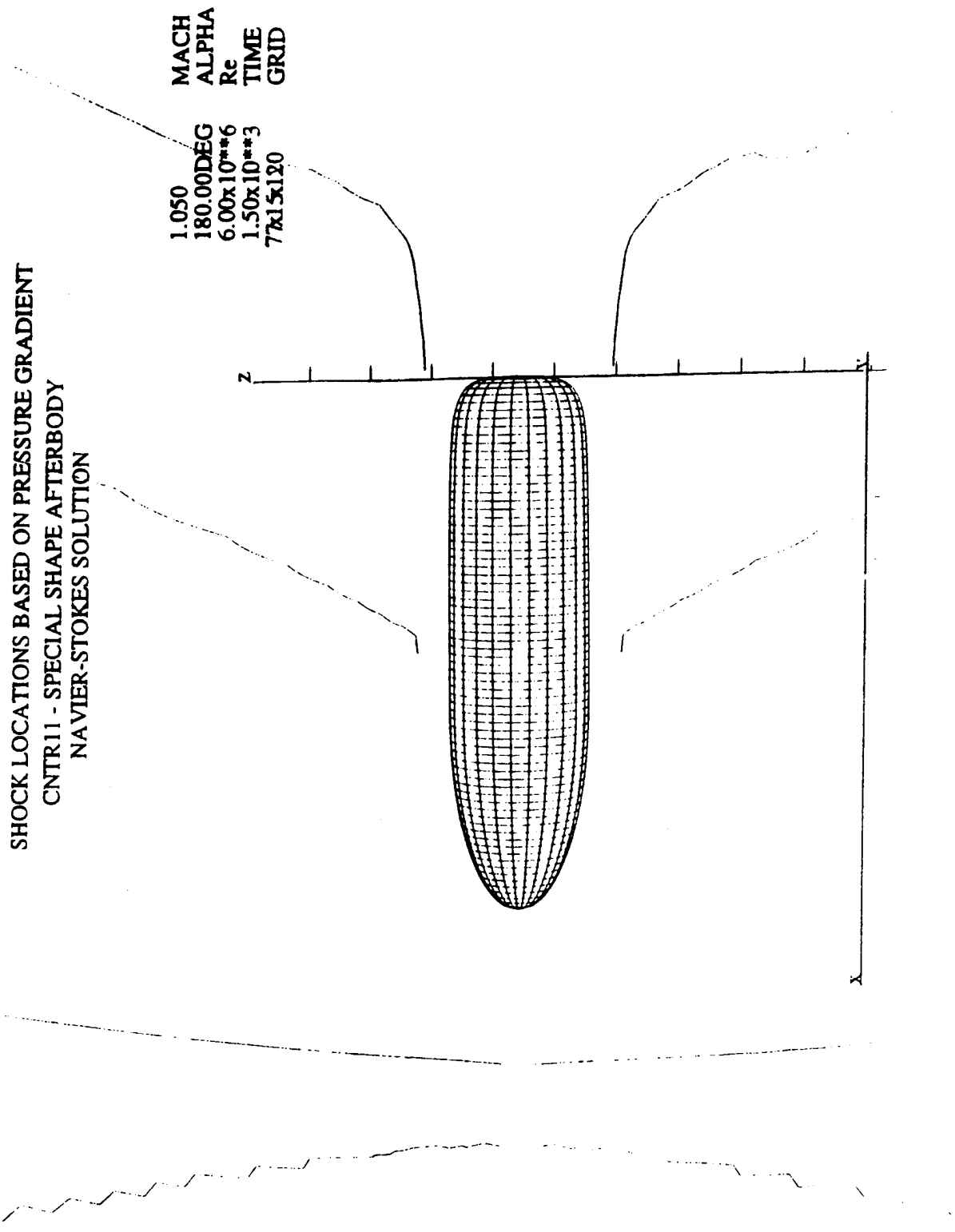
SHOCK LOCATIONS BASED ON PRESSURE GRADIENT
CNTR11 - SPECIAL SHAPE AFTERBODY
NAVIER-STOKES SOLUTION
MACH 1.050
ALPHA 180.00DEG
Re 6.00x10**6
TIME 1.50x10**3
GRID 77x15x120
Z
Y
X

Figure 12

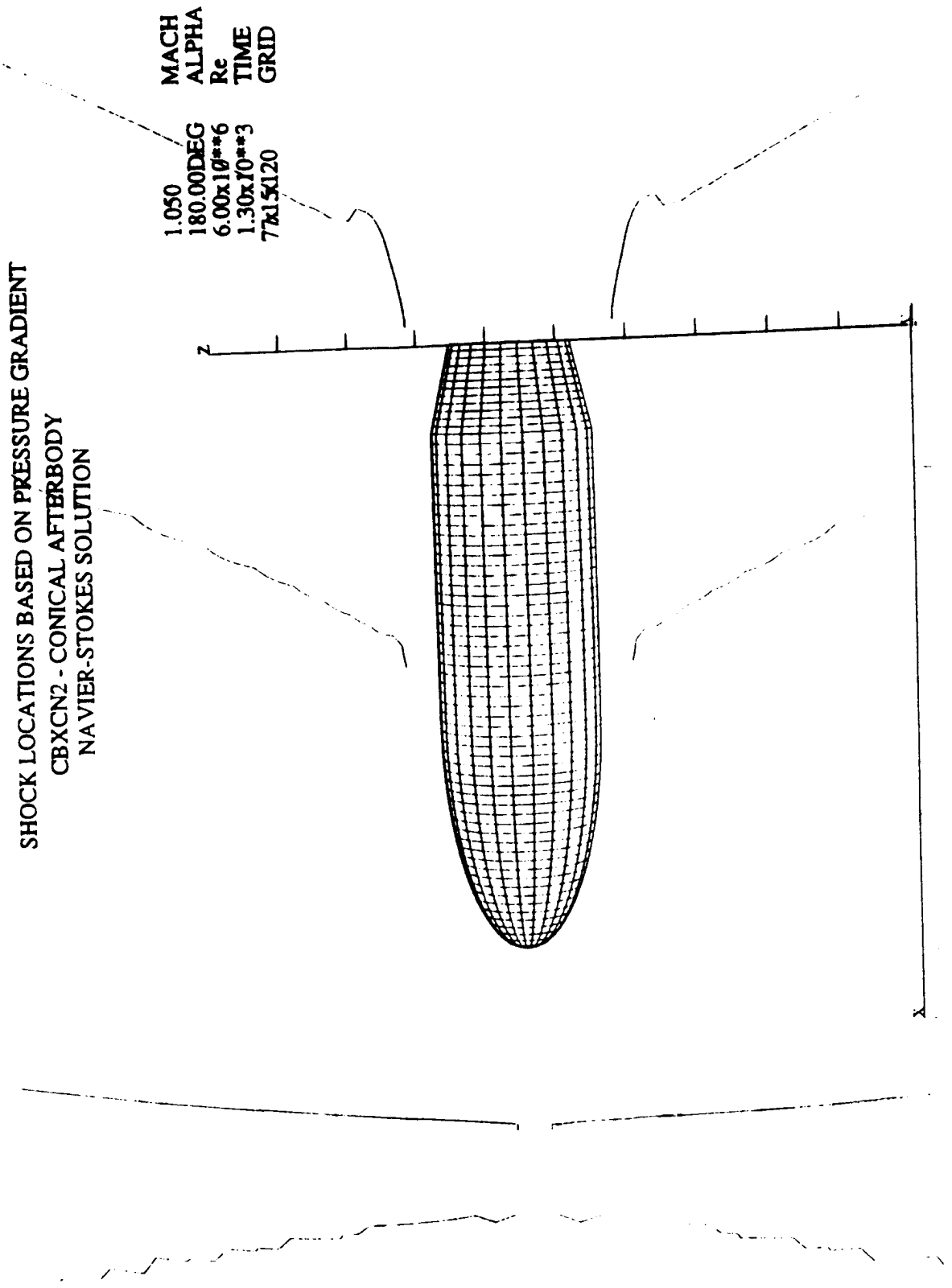
SHOCK LOCATIONS BASED ON PRESSURE GRADIENT
CBXCN2 - CONICAL AFTERBODY
NAVIER-STOKES SOLUTION
MACH 1.050
ALPHA 180.00DEG
Re 6.00x10**6
TIME 1.30x10**3
GRID 7x15x120
Z
X

Figure 13

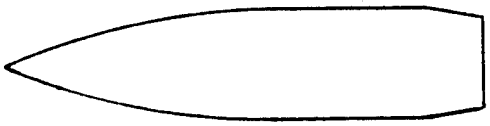

M = 0.84

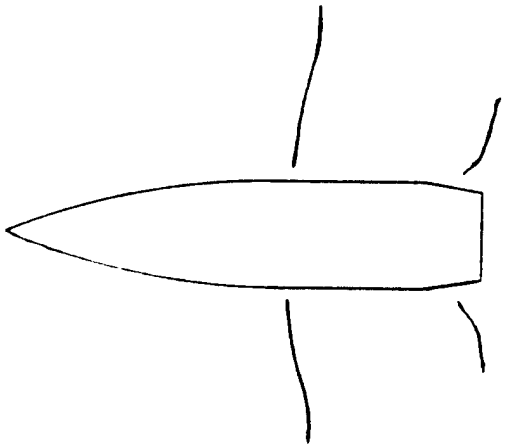

M = 0.946

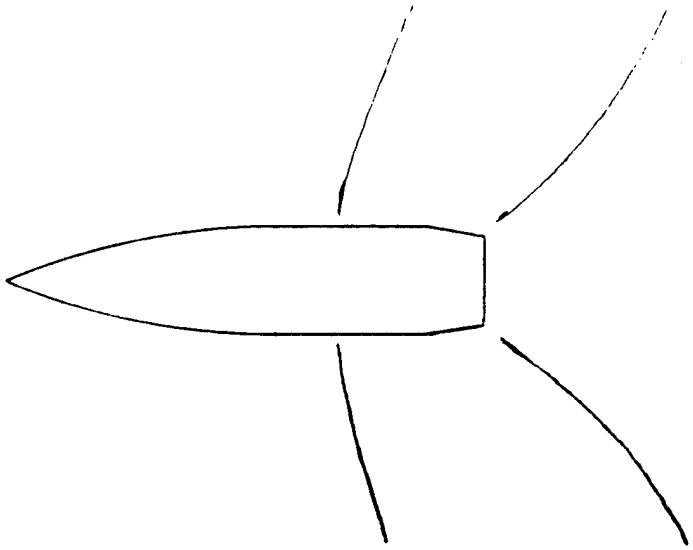

M = 1.015

Figure 14

APPENDIX B. FORTRAN PROGRAMS AND OVERFLOW INPUT FILE

```
************************************************************************
*                                                                      *
*                            D2D3.F                                    *
*    This FORTRAN program will prepare a formatted 2-D grid            *
*    data file for processing by ROTATEGR.F                            *
*                                                                      *
************************************************************************

      real X(77,120),Y(77,120),Z(77,120)
      open(unit=12,file='grid2d.for',status='unknown')
      open(unit=14,file='cone3d.for',status='new')
      READ(12,*)  IDIM,JDIM
      READ(12,*)  ((X(I,J),I=1,IDIM),J=1,JDIM),
     +            ((Y(I,J),I=1,IDIM),J=1,JDIM)
      Z(I,J)=0.0
      WRITE(14,*) IDIM,JDIM,1
      WRITE(14,*) ((X(I,J),I=1,IDIM),J=1,JDIM),
     +            ((0.0,I=1,IDIM),J=1,JDIM),
     +            ((Y(I,J),I=1,IDIM),J=1,JDIM)
      STOP
      END



************************************************************************
*                                                                      *
*                          ROTATEGR.F                                  *
*     This FORTRAN program takes a formatted 2-D grid and              *
*     generates an Axi-Symmetric an unformatted 3-D grid               *
*     Converts grid2d.for to cone.for                                  *
*                                                                      *
************************************************************************

      dimension  x(77,120),   y(77,120),   z(77,120)
      dimension xx(77,15,120), yy(77,15,120), zz(77,15,120)
      character*30 fni
      character*30 fno
      print *, 'Input 2-D grid filename'
      read (*,21) fni
      rewind 2
      open (2,file=fni,form='formatted')
      read (2,*) i1,j1,k1
      read (2,*) (( x(i,j),i=1,i1),j=1,j1),
     +           (( y(i,j),i=1,i1),j=1,j1),
     +           (( z(i,j),i=1,i1),j=1,j1)
      close(2)
      pi = 4.*atan(1.)
      print *, 'No of Planes in j dir ? '
      read (5,*) jm
      dth = (180. / (jm-1)) * (pi/180.)
      do 11 i = 1,i1
      do 11 j = 1,j1
      k=j
      xx(i,2,k) = x(i,k)
      yy(i,2,k) = 0.
      zz(i,2,k) = z(i,k)
11    continue
```

```
      im=i1
      km=j1
      do 20 j=3,jm+1
      do 20 i=1,im
      do 20 k=1,km
      xx(i,j,k) = x(i,k)
      th = (j-2)*dth
      yy(i,j,k) = sin(th)*z(i,k)
      zz(i,j,k) = cos(th)*z(i,k)
20    continue
      do 30 i=1,im
      do 30 k=1,km
      j=1
      xx(i,j,k) = xx(i,j+2,k)
      yy(i,j,k) =-yy(i,j+2,k)
      zz(i,j,k) = zz(i,j+2,k)
      j=jm+2
      xx(i,j,k) = xx(i,j-2,k)
      yy(i,j,k) = -yy(i,j-2,k)
      zz(i,j,k) = zz(i,j-2,k)
30    continue
      jm = jm+2
      print *, 'Output 3-D grid filename  ='
      read (5,21) fno
      rewind 3
      open ( 3, file=fno,form='unformatted')
      write (3) im,jm,km
      write (3) ((( xx(i,j,k), i=1,im), j=1,jm),k=1,km),
     +          ((( yy(i,j,k), i=1,im), j=1,jm),k=1,km),
     +          ((( zz(i,j,k), i=1,im), j=1,jm),k=1,km)
      close (3)
      stop
      end
```

```
************************************************************************
*                              READX.F                                 *
*    This FORTRAN program will read formatted data files and           *
*    convert them to unformatted binary data files for input           *
*    into OVERFLOW  - Converts grid.for to grid.in                     *
************************************************************************

 real x(77,15,120),y(77,15,120),z(77,15,120)
 open(unit=12,file='grid.for',status='unknown')
 open(unit=14,file='grid.in',status='new',form='unformatted')
 read(12,*) IDIM,JDIM,KDIM
 read(12,*) (((X(I,J,K),I=1,IDIM),J=1,JDIM),K=1,KDIM),
+           (((Y(I,J,K),I=1,IDIM),J=1,JDIM),K=1,KDIM),
+           (((Z(I,J,K),I=1,IDIM),J=1,JDIM),K=1,KDIM)
 write(14)  IDIM,JDIM,KDIM
 write(14)  (((X(I,J,K),I=1,IDIM),J=1,JDIM),K=1,KDIM),
+           (((Y(I,J,K),I=1,IDIM),J=1,JDIM),K=1,KDIM),
+           (((Z(I,J,K),I=1,IDIM),J=1,JDIM),K=1,KDIM)
 stop
 end
```

```
************************************************************************
*                              READQ.F                                 *
* This FORTRAN program will read unformatted binary data               *
* files and convert them to formatted data files for input             *
* into PLOT3D - Converts q.save to q.form                              *
************************************************************************

 dimension q(77,15,120,5)
 open(unit=1,file='q.save',status='unknown',form='unformatted')
 open(unit=20,file='q.form', status='new',form='formatted')
 read(1) ni, nj, nk
 read(1)fsmach,alpha,re,time
 read(1)((((q(i,j,k,nx),i=1,ni),j=1,nj),k=1,nk),nx=1,5)
 write(20,*) ni, nj, nk
 write(20,*)fsmach,alpha,re,time
 write(20,*)((((q(i,j,k,nx),i=1,ni),j=1,nj),k=1,nk),nx=1,5)
 print*, ni, nj, nk
 stop
 end
```

```
            INPUT FILE FOR OVERFLOW (OVERFLOW.IN)
            *************************************
$GLOBAL
  CHIMRA = .F.,   NSTEPS = 1000, RESTRT = .F.,   NSAVE = 100,
  NQT    = 0,
  $END
$FLOINP
  ALPHA  = 180.0, FSMACH = 0.95,    REY = 6.00E6, TINF = 520.0,
  $END
$VARGAM
  $END
$GRDNAM
  NAME   = 'Half complete body, CNTR11 , 77x15x120 Grid',
$END
$NITERS
  $END
$METPRM
  IRHS   = 0,       ILHS = 2,  IDISS = 2,
  $END
$TIMACU
  DT     = 0.01, ITIME = 1   TFOSO = 1.00,  CFLMIN = 3.0,
  $END
$SMOACU
  ISPECJ = 2,  DIS2J = 2.00,  DIS4J = 0.02,
  ISPECK = 2,  DIS2K = 2.00,  DIS4K = 0.02,
  ISPECL = 2,  DIS2L = 2.00,  DIS4L = 0.02,
  SMOO   = 1.00,
  EPSE   = 0.35,
  $END
$VISINP
  VISCJ = .T.,  VISCK = .T.,  VISCL = .T.,
  NTURB =   2,
  ITTYP =   1,  11,
  ITDIR =   3,   3,
  JTLS  =  -1,   1,
  JTLE  =   1,  -1,
  KTLS  =   1,   1,
  KTLE  =  15,  15,
  LTLS  =   1,   1,
  LTLE  =  -1,  -1,
  TLPAR1= 0.9,   1,
  $END
$BCINP
  NBC   =     6,
  IBTYP =    15,  15,   12,   12,    5,   32,
  IBDIR =     1,  -1,    2,   -2,    3,   -3,
  JBCS  =     1,  77,    1,    1,    1,    1,
  JBCE  =     1,  77,   77,   77,   77,   77,
  KBCS  =     1,   1,    1,   15,    1,    1,
  KBCE  =    15,  15,    1,   15,   15,   15,
  LBCS  =     1,   1,    1,    1,    1,  120,
  LBCE  =   120, 120,  120,  120,    1,  120,
  $END
$SCEINP
$END
```

APPENDIX C. TABLE OF OVERFLOW INPUTS

MODEL	M_∞	DT	CFLMIN	NO. OF ITERATIONS
CBXCN2	0.95	0.01	3.0	1000
		0.01	5.0	500
		0.01	7.0	500
		0.01	8.0	500
CBXCN2	1.2	0.01	3.0	1000
		0.01	2.0	200
		0.03	3.0	300
CNTR11	0.8	0.01	3.0	500
		0.01	5.0	1000
CNTR11	0.95	0.01	3.0	1000
		0.1	2.0	200
		0.1	3.0	200
		0.005	5.0	800
CNTR11	1.05	0.01	3.0	1000
		0.01	5.0	500

TABLE 1

INITIAL DISTRIBUTION LIST

		No. Copies
1.	Defense Technical Information Cameron Station Alexandria, Virginia 22304-6145	2
2.	Library, Code 52 Naval Postgraduate School Monterey, California 93943-5101	2
3.	Chairman Department of Aeronautics, Code AA/Co Naval Postgraduate School Monterey, California 93943-5101	1
4.	Prof. O. Biblarz, Code AA/Bi Naval Postgraduate School Monterey, California 93943-5101	3
5.	Prof. G. Hobson, Code AA/Hg Naval Postgraduate School Monterey, California 93943-5101	1
6.	Major Fan, Yue Sang Air Logistics Department HQ Republic of Singapore Airforce MINDEF Building, Gombak Drive SINGAPORE 2366 Republic of Singapore	2